Study of Aerothermodynamic Modeling Issues Relevant to High-Speed Sample Return Vehicles

Christopher O. Johnston
NASA Langley Research Center
Hampton, VA 23681-2199
USA

Christopher.O.Johnston@nasa.gov

ABSTRACT

This paper examines the application of state-of-the-art coupled ablation and radiation simulations to high-speed sample return vehicles, such as those returning from Mars or an asteroid. A defining characteristic of these entries is that the surface recession rates and temperatures are driven by nonequilibrium convective and radiative heating through a boundary layer with significant surface blowing and ablation products. Measurements relevant to validating the simulation of these phenomena are reviewed and the Stardust entry is identified as providing the best relevant measurements. A coupled ablation and radiation flowfield analysis is presented that implements a finite-rate surface chemistry model. Comparisons between this finite-rate model and a equilibrium ablation model show that, while good agreement is seen for diffusion-limited oxidation cases, the finite-rate model predicts up to 50% lower char rates than the equilibrium model at sublimation conditions. Both the equilibrium and finite rate models predict significant negative mass flux at the surface due to sublimation of atomic carbon. A sensitivity analysis to flowfield and surface chemistry rates show that, for a sample return capsule at 10, 12, and 14 km/s, the sublimation rates for C and C_3 provide the largest changes to the convective flux, radiative flux, and char rate. A parametric uncertainty analysis of the radiative heating due to radiation modeling parameters indicates uncertainties ranging from 27% at 10 km/s to 36% at 14 km/s. Applying the developed coupled analysis to the Stardust entry results in temperatures within 10% of those inferred from observations, and final recession values within 20% of measurements, which improves upon the 60% over-prediction at the stagnation point obtained through an uncoupled analysis. Emission from CN Violet is shown to be over-predicted by nearly and order-of-magnitude, which is consistent with the results of previous independent analyses. Finally, the coupled analysis is applied to a 14 km/s Earth entry representative of a Mars sample return. Although the radiative heating provides a larger fraction of the total heating, the influence of ablation and radiation on the flowfield are shown to be similar to Stardust.

1.0 INTRODUCTION

NASA's current plans for solar system exploration will require thermal protection systems (TPS) that can withstand the heating environment resulting from Earth entry velocities between 12 and 18 km/s. For example, several concepts for Mars sample return are presently being developed, which typically consist of a Stardust-like capsule ($\sim$1.0 m maximum diameter) entering Earth at around 14 km/s, with peak heating at around 12.5

km/s and 65 km. As another example, the OSIRIS-REx mission plans to return a piece of a potentially Earth-threatening asteroid using a Stardust-like capsule. The entry conditions for this mission are similar to Stardust. The most challenging of all the presently proposed high speed Earth entries results from proposed sample return missions from Saturn's moon Enceladus [1], which require Earth entry velocities between 16 and 18 km/s. Considering a larger re-entry vehicle, the Inspiration Mars mission [2] proposes to return an Orion-sized ($\sim$5 m radius) capsule to Earth at 14.2 km/s, which would result in peak heating around 65 km at a velocity of 13.5 km/s.

These challenging missions, among others, provide motivation for the improved understanding of aerothermodynamic environments relevant to Earth entries at hyperbolic velocities (V >12 km/s). At these high velocities, the coupling between shock layer radiation, surface char, in-depth pyrolysis, convective heating, and flowfield chemistry become significant. The accurate modeling of these coupled phenomena are required for efficient TPS design. As first steps towards assessing the simulation uncertainty for these high velocity missions, a review of relevant flight and laboratory data, development of a baseline simulation approach, and sensitivity analysis of the developed approach are needed. These tasks are the subject of the present paper.

Section 2 provides an overview of existing flight and laboratory data relevant to high-speed Earth entry. Convective heating, radiative heating, and surface recession measurements are discussed along with the results of past attempts to simulate these data using coupled radiation and ablation flowfield analyses. Following this discussion, Section 3 presents the baseline model applied in this work, which represents a state-of-the-art coupled ablation and radiation flowfield analysis. A comparison between equilibrium ablation and finite-rate surface chemistry is presented in Section 4 to provide insight into the differences between the two models. To provide guidance for future uncertainty analyses, Section 5 presents a sensitivity analysis of the convective heating, radiative heating, and char rate, to changes in surface and flowfield reaction rates, as well as radiation modeling parameters. Section 6 applies the developed analysis to the Stardust entry, which allows for a comparison with the final surface recession, inferred surface temperatures, and observed radiative emissions. As a final example, Section 7 presents a coupled analysis of an Earth entry trajectory representative of a Mars sample return at 14 km/s.

2.0 OVERVIEW OF RELEVANT MEASUREMENTS

To guide the simulations presented in this paper, this section reviews existing experimental data relevant to high-speed Earth entry, and particularly sample return missions. The smaller nose radius for a sample return mission ($\approx$0.3 m) relative to a manned mission ($\approx$3.0 m) results in mostly laminar flow and a smaller influence of radiation. A review of measurements relevant to manned missions is presented by Johnston et al. [3–5]. The current review will focus on measurements relevant to the forebody of sample return missions, with the discussion of the afterbody presented in a separate paper by Johnston and Brandis [6].

2.1 Stardust and Hayabusa

The Stardust (0.81 m maximum diameter and 0.23 m nose radius entering at 12.2 km/s) and Hayabusa (0.40 m maximum diameter and 0.20 m nose radius entering at 11.7 km/s) missions represent successful entries at the lower end of the velocity range of present interest. Unfortunately, no heat shield instrumentation was included on these vehicles, so the only relevant aerothermodynamic flight data are the final heat shield recession and in-depth properties obtained from the recovered heat shields [7, 8] along with the observed radiation signal measured from a distant aircraft [9–13]. For both vehicles, post-flight analyses [8, 14] indicate that the recession is dominated by diffusion-limited oxidation (sublimation may occur very briefly near peak heating), which

is relatively independent of surface temperature. This weak relationship between surface temperature and recession makes it difficult to assess the convective heating simulation quality based on a comparison of the simulated and measured recession values. Nevertheless, Kontinos and Stackpoole [7] show that an uncoupled ablation analysis over-predicts the measured Stardust recession by 60%, while Suzuki et al. [8] report a factor of 3 over-prediction of the measured Hayabusa recession using a coupled ablation analysis. These over-predictions are assumed to result from uncertainties in the surface ablation models.

The observed radiation signals measured from a distant aircraft provide additional insight into the convective heating uncertainty. These radiation measurements provide the blackbody emission from the heat shield (along with the weaker emission from the shock layer gas), which allows the surface temperature of the vehicle to be inferred. For Stardust entry, Trumble [14] and Winter [9] show that an uncoupled ablation analysis over-predicts the inferred surface temperatures by 100 K. For Hayabusa entry, Yamada et al. [13] over-predict the measured temperature by 500 K in the early phase of the trajectory (which contains significant thermochemical nonequilibrium), while under-predicting by 200 K late in the trajectory.

In addition to inferring the surface temperatures and therefore the dominant convective heating, the observed radiation signals provide insight into the radiation from the shock layer gas. Two notable insights are obtained from previous studies of these measurements. The first insight obtained by Liu et al. [15], who simulated the measurements using ray-tracing with the NEQAIR radiation code on non-ablating DPLR flowfield simulations, shows an under-prediction of atomic oxygen lines between 700 – 900 nm, while good agreement is seen for the atomic nitrogen lines. The second insight, obtained by Winter and Trumble [9], shows that CN Violet emission occurs at vibrational temperatures characteristic of the inviscid region of the shock layer, which is unexpected because CN is an ablation product and expected to remain in the lower temperature boundary layer. While the first of these insights is studied further by Johnston and Brandis [6], which is shown to relate to emission from the nonequilibrium afterbody flow, the second of these insights will be reinterpreted later in this paper using a coupled ablation analysis.

2.2 Fire II

The widely studied Fire II experiment [16] (0.67 m maximum diameter and 0.93 m nose radius entering at 11.36 km/s) provides calorimeter measurements of the convective plus absorbed radiative heating for a non-ablating Beryllium heat shield. Coupled radiation computations by Johnston et al. [17], among others, show that simulations agree within $\pm 20\%$ of the measurements. For the forebody, simulations indicate that convective heating contributes more than 70% of the total calorimeter measurement, which suggests that these comparisons are more relevant for assessing the quality of the convective heating than the radiative heating. However, as shown by Johnston and Brandis [6], the calorimeters on the *afterbody* actually experience a greater fraction of radiative heating than the forebody.

Fire II total radiometer measurements provide spectrally-integrated radiative intensity measurements between 200 – 4000 nm. Coupled radiation simulations by Johnston et al. [17] agree within $\pm 30\%$ of the stagnation region flight measurements. Because no spatial or spectral resolution is available for the measurements, this good agreement does not provide conclusive validation of the nonequilibrium radiative heating simulations at these conditions.

Parametric uncertainty analyses for Fire II convective heating are presented by Kleb et al. [18] and Palmer [19], although they both treat all uncertainties as aleatory, which leads to uncertainties that are erroneously small. Both studies found convective heating parametric uncertainties of roughly $\pm 5\%$ for Fire II peak heating. For the radiative heating, Johnston and Kleb [20] computed a parametric uncertainty of $\pm 30\%$ using an approach that treats all uncertainties as epistemic. A similar approach is applied in Section 5.2 of this paper.

2.3 Shock Tube

Comparisons between simulations and EAST measurements in air between 9.5 to 15.5 km/s are shown by Brandis et al. [21] to be between $\pm 30\%$ for equilibrium emission. This value agrees with the values computed through a parametric uncertainty analysis by Johnston et al. [5]. These data and analyses indicate that uncertainty in equilibrium air radiation is presently no greater than $\pm 30\%$ using the HARA or NEQAIR codes. However, nonequilibrium air radiation, which provides the dominant contribution to afterbody radiation, contains significantly larger uncertainties. Studies by Johnston [22], Panesi et al. [23], Potter [24], and Lemal [25] show that comparisons with the nonequilibrium radiance profiles measured in EAST provide inconclusive validation for the chemical kinetic and non-Boltzmann models. Because nonequilibrium radiation has a small influence on manned Earth entry programs, such as Orion, the motivation to improve these comparisons has been limited. However, for the smaller sample-return vehicles studied in this work, the impact of nonequilibrium emission, particularly that from N_2^+ First-Negative, is not negligible.

2.4 Other Relevant Measurements

Recent arc-jet measurements have been the used to validate finite-rate surface models [26, 27] for PICA. These comparisons show good agreement between the measured recession and coupled ablation simulations using the modified Park model [28], which replaces the originally proposed nitridation reaction with nitrogen recombination. Pyrolysis gases were assumed to be in chemical equilibrium at the wall temperature and pressure. Surface temperatures for these comparisons ranged from 1600–3100 K, which indicates that the temperatures were just below the sublimation-dominated regime and therefore dominated by diffusion-limited oxidation. Because the recession rate in the diffusion-limited oxidation regime is essentially independent of the oxidation rate, these comparisons do not provide sufficient validation of the oxidation rate. However, they do provide confidence in the application of the ablating boundary condition and the assumption of equilibrium pyrolysis gases.

Plasmatron studies by Helber et al. [29] provide spectral measurements of ablation product emission in the boundary layer for surface temperatures up to 2800 K. Significant CN Violet emission is seen, which is consistent with Stardust measurements.

3.0 BASELINE SIMULATION APPROACH

Most of the relevant details of the present coupled radiation and ablation simulation approach are presented by Johnston et al. [30]. The only difference in the present approach is that a finite-rate surface model is applied, instead of the equilibrium ablation model, to compute the char rate. The rates for this finite-rate surface model are presented after a brief review of the flowfield model, including chemical kinetics, radiation model, and governing surface equations.

3.1 Flowfield Modeling

The LAURA v5 Navier-Stokes solver[31] was applied in this work, which includes a two-temperature thermochemcial nonequilibrium model, as presented by Gnoffo et al. [32]. This code has been applied to a wide variety of NASA missions [33] since its development in the 1980s [34], and has undergone significant validation. For the cases considered in this work with coupled ablation, the following 27 species are treated throughout the flowfield: N, N^+, NO, NO^+, N_2, N_2^+, O, O^+, O_2, O_2^+, e^-, C, C^+, CO, CO^+, CO_2, C_2, C_3, C_5, C_2H, C_2H_2, CN, H, H^+, H_2, HCN, CH. The thermodynamic properties for these species are obtained from Gordon and Mcbride[35]. The transport properties are obtained from Wright et al.[36, 37] where available. The

Table 1: Chemical kinetics for air species applied in the present baseline model.

i	Reaction	$A_{f,i}$	$n_{f,i}$	$D_{f,i}$	$T_{f,i}$	Third Body, M	Ref.
1	$N_2 + M \leftrightarrow 2N + M$	3.0e+22	-1.60	1.132e+5	T_a	N, C, O	Park [41]
		6.0e+3	2.6	1.132e+5	T_{ve}	e^-	Bourdon et al. [42]
		7.0e+21	-1.60	1.132e+5	T_a	others	Park [41]
1	$NO + M \leftrightarrow N + O + M$	4.40+16	0.00	7.55e+4	T_a	N, C, O, NO, CO_2	Park [41]
		2.0e+15	0.00	7.55e+4	T_a	others	Park [41]
3	$O2 + M \leftrightarrow 2O + M$	1.0e+22	-1.50	5.936e+4	T_a	N, C, O	Park [41]
		2.0e+21	-1.50	5.936e+4	T_a	others	Park [41]
4	$N_2 + O \leftrightarrow NO + N$	6.0e+13	0.1	3.80e+4	T_{tr}		Fujita et al. [43]
5	$O_2 + N \leftrightarrow NO + O$	2.49e+9	1.18	4.01e+3	T_{tr}		Bose & Candler [44]
6	$N + O \leftrightarrow NO^+ + e^-$	5.30e+12	0.0	3.19e+4	T_{tr}		Park et al. [45]
7	$NO^+ + N \leftrightarrow O^+ + N_2$	3.40e+13	-1.08	1.28e+4	T_{tr}		Park [41]
8	$NO^+ + O \leftrightarrow O_2^+ + N$	7.20e+12	0.29	4.86e+4	T_{tr}		Park [41]
9	$NO^+ + O_2 \leftrightarrow NO + O_2^+$	2.40e+13	0.41	3.26e+4	T_{tr}		Park [41]
10	$O + O \leftrightarrow O_2^+ + e^-$	7.10e+02	2.7	8.06e+4	T_{tr}		Park [45]
11	$O + e^- \leftrightarrow O^+ + 2e^-$	3.90e+33	-3.78	1.585e+5	T_{ve}		Park [41]
12	$O_2^+ + O \leftrightarrow O^+ + O_2$	4.00e+12	-0.09	1.80e+4	T_{tr}		Park [45]
13	$O_2 + e^- \leftrightarrow O_2^+ + 2e^-$	2.19e+10	1.16	1.30e+5	T_{ve}		Teulet et al. [46]
14	$N + N \leftrightarrow N_2^+ + e^-$	4.40e+07	1.50	6.750e+4	T_{tr}		Park [28]
15	$N + e^- \leftrightarrow N^+ + e^- + e^-$	2.50e+34	-3.82	1.682e+5	T_{ve}		Park [28]
16	$N^+ + N2 \leftrightarrow N_2^+ + N$	1.00e+12	0.50	1.220e+4	T_{tr}		Bourdon et al. [42]
17	$N2 + O^+ \leftrightarrow N_2^+ + O$	9.10e+11	0.36	2.280e+4	T_{tr}		Park [45]
18	$N2 + e^- \leftrightarrow 2N + e^-$	6.00e+3	2.6	1.132e+5	T_{ve}		Bourdon et al. [42]
19	$NO + O^+ \leftrightarrow N^+ + O2$	1.40e+05	1.90	2.660e+4	T_{tr}		Park [45]
20	$NO^+ + C \leftrightarrow C^+ + NO$	1.00e+13	0.0	2.32e+4	T_{tr}		Fujita et al. [43]
21	$NO^+ + N \leftrightarrow N_2^+ + O$	7.20e+13	0.00	3.550e+4	T_{tr}		Park [45]
22	$NO^+ + N \leftrightarrow O^+ + N2$	3.40e+13	-1.08	1.280e+4	T_{tr}		Park [45]
23	$NO^+ + O \leftrightarrow N^+ + O2$	1.00e+12	0.50	7.720e+4	T_{tr}		Park [45]
24	$NO^+ + O \leftrightarrow O_2^+ + N$	7.20e+12	0.29	4.860e+4	T_{tr}		Fujita et al. [43]
25	$NO^+ + O2 \leftrightarrow NO + O_2^+$	2.40e+13	0.41	3.260e+4	T_{tr}		Park [45]
26	$O_2^+ + N \leftrightarrow O2 + N^+$	8.70e+13	0.14	2.860e+4	T_{tr}		Park [45]
27	$O_2^+ + N2 \leftrightarrow N_2^+ + O2$	9.90e+12	0.00	4.070e+4	T_{tr}		Park [45]

remaining species are treated using the approximate approach of Svehla[38] modified as suggested by Park[28]. The chemical reaction rates applied, which are the same as those used by Johnston et al. [30, 39], are listed in Tables 1 and 2. Note that the species and rates applied here are significantly reduced from those proposed by Martin and Boyd [40]. The additional species suggested by Martin and Boyd were found to have a negligible impact on the radiative and convective heating for the cases studied in this work, which may not be true for all cases.

The standard approach to coupling radiation to the flowfield [51] involves adding the divergence of the radiative flux (Δq_r), obtained from the HARA radiation code discussed in the next subsection, into the vibrational-electronic and total energy equations. To avoid numerical instabilities, Δq_r is typically set to zero in the free-stream. Although this approach will be applied for the standard coupled radiation simulations presented in this work, a more advanced approach is considered by Johnston et al. [30], which accounts for precursor absorption. The impact of the precursor on the present sample return cases is negligible, even at 15 km/s, because of the small vehicle size, which reduces the volume of the shock layer gas radiating into the free-stream.

3.2 Radiation Modeling

Radiation computations in this work are made using the state-of-the-art HARA radiation code, which is coupled to LAURA flowfield code and included in standard LAURA releases [52]. HARA was developed for *efficient*

Table 2: Chemical kinetics for ablation products applied in the present baseline model.

i	Reaction	$A_{f,i}$	$n_{f,i}$	$D_{f,i}$	$T_{f,i}$	Third Body, M	Ref.
1	$CO_2 + M \leftrightarrow CO + O + M$	1.38e+22	-1.50	6.328e+4	T_a	N, C, O	Johnston et al. [47]
		6.9e+20	-1.50	6.328e+4	T_a	Ar	Johnston et al. [47]
		6.9e+21	-1.50	6.328e+4	T_a	others	Johnston et al. [47]
2	$CO + M \leftrightarrow C + O + M$	1.80e+21	-1.00	1.29e+5	T_a	N, C, O	Johnston et al. [47]
		1.20e+20	-1.00	1.29e+5	T_a	Ar	Johnston et al. [47]
		1.20e+21	-1.00	1.29e+5	T_a	others	Johnston et al. [47]
3	$C_2 + M \leftrightarrow 2C + M$	4.5e+18	-1.00	7.15e+4	T_a	All	Johnston et al. [47]
4	$CN + M \leftrightarrow C + N + M$	6.0e+15	-0.4	7.10e+4	T_a	All	Fujita et al. [43]
8	$CO_2 + O \leftrightarrow O_2 + CO$	2.71e+14	0.0	3.38e+4	T_{tr}		Ibragimova [48]
9	$CO + C \leftrightarrow C_2 + O$	2.4e+17	-1.00	5.80e+4	T_{tr}		Park et al. [49]
10	$CO + N \leftrightarrow CN + O$	1.0e+15	0.00	3.86e+4	T_{tr}		Johnston et al. [47]
11	$CO + NO \leftrightarrow CO_2 + N$	3.0e+6	0.88	1.33e+4	T_{tr}		Fujita et al. [43]
12	$CO + O \leftrightarrow O_2 + C$	3.9e+13	-0.18	6.92e+4	T_{tr}		Park et al. [49]
13	$C_2 + N_2 \leftrightarrow CN + CN$	1.5e+13	0.0	2.1e+4	T_{tr}		Gokcen [50]
14	$CN + C \leftrightarrow C_2 + N$	3.0e+14	0.00	1.81e+4	T_{tr}		Fujita et al. [43]
15	$CN + O \leftrightarrow NO + C$	1.6e+12	0.10	1.46e+4	T_{tr}		Johnston et al. [47]
16	$N + CO \leftrightarrow NO + C$	1.1e+14	0.07	5.35e+4	T_{tr}		Fujita et al. [43]
17	$N_2 + C \leftrightarrow CN + N$	1.1e+14	-0.11	2.32e+4	T_{tr}		Park et al. [49]
18	$N_2 + CO \leftrightarrow CN + NO$	1.2e+16	-1.23	7.70e+4	T_{tr}		Fujita et al. [43]
19	$C_2 + C_2H_2 \leftrightarrow 2C_2H$	1.10e+14	-0.38	6.87e+3	T_{tr}		Fujita et al. [43]
20	$C_2H + H \leftrightarrow C_2 + H_2$	1.60e+13	0.15	1.460e+4	T_{tr}		Fujita et al. [43]
21	$C_2H + M \leftrightarrow C_2 + H + M$	1.70e+35	-5.16	5.74e+4	T_a		Fujita et al. [43]
22	$C_2H_2 + M \leftrightarrow C_2H + H + M$	4.00e+16	0.0	5.40e+4	T_a		Fujita et al. [43]
23	$C_3 + C \leftrightarrow C_2 + C_2$	6.00e+11	1.07	1.650e+4	T_{tr}		Fujita et al. [43]
24	$C_3 + M \leftrightarrow C_2 + C + M$	1.60e+21	-1.5	8.774e+4	T_a	H, C, N, O	Fujita et al. [43]
		8.40e+20	-1.5	8.774e+4	T_a	others	Fujita et al. [43]
25	$C_3 + N \leftrightarrow CN + C_2$	1.00e+12	0.00	3.420e+4	T_{ve}		Park [28]
26	$C_5 + M \leftrightarrow C_3 + C_2 + M$	4.00e+14	0.0	81549.0	T_a		Johnston et al. [47]
27	$CH + C \leftrightarrow C_2 + H$	2.00e+14	0.0	0.0	T_{tr}		Gokcen [50]
28	$CH + CO \leftrightarrow C_2H + O$	2.50e+10	0.67	3.90e+4	T_{tr}		Fujita et al. [43]
29	$CH + M \leftrightarrow C + H + M$	1.90e+14	0.0	3.3717e+4	T_a		Fujita et al. [43]
30	$CH + N_2 \leftrightarrow HCN + N$	4.40e+12	0.0	1.106e+4	T_{tr}		Gokcen [50]
31	$CN + H_2 \leftrightarrow HCN + H$	2.95e+05	0.0	1.13e+3	T_{tr}		Gokcen [50]
32	$CO + C_2 \leftrightarrow C_3 + O$	1.00e+12	0.00	4.120e+4	T_{ve}		Park [28]
33	$H + C_2H_2 \leftrightarrow C_2H + H_2$	1.00e+16	-0.5	1.55e+4	T_{tr}		Fujita et al. [43]
34	$H + CN \leftrightarrow CH + N$	1.50e+15	-0.12	4.976e+4	T_{tr}		Fujita et al. [43]
35	$H + CO \leftrightarrow CH + O$	6.70e+14	0.15	8.847e+4	T_{tr}		Fujita et al. [43]
36	$H_2 + C \leftrightarrow CH + H$	4.00e+14	0.00	1.17e+4	T_{tr}		Fujita et al. [43]
37	$H_2 + M \leftrightarrow 2H + M$	9.0e+14	0.00	4.840e+4	T_a		Fujita et al. [43]
38	$HCN + M \leftrightarrow CN + H + M$	3.57e+26	-2.60	6.2845e+4	T_a		Gokcen [50]
39	$C + O \leftrightarrow CO^+ + e^-$	8.8e+8	1.0	3.31e+4	T_{tr}		Park et al. [49]
40	$C + e^- \leftrightarrow C^+ + 2e^-$	3.9e+33	-3.78	1.307e+5	T_{ve}		Park et al. [49]
41	$C^+ + CO \leftrightarrow CO^+ + C$	1.0e+13	0.0	3.14e+4	T_{tr}		Park et al. [49]
42	$CO + e^- \leftrightarrow CO^+ + 2e^-$	4.5e+14	0.275	1.63e+5	T_{ve}		Teulet et al. [46]
43	$NO^+ + C \leftrightarrow C^+ + NO$	1.0e+13	0.0	2.32e+4	T_{tr}		Park et al. [49]
44	$O_2 + C^+ \leftrightarrow O_2^+ + C$	1.00e+13	0.0	9.40e+3	T_{tr}		Park et al. [49]
45	$C + N \leftrightarrow CN^+ + e^-$	1.00e+15	1.50	1.6444e+5	T_{tr}		Gokcen [50]
46	$C^+ + N_2 \leftrightarrow N_2^+ + C$	1.11e+14	-0.11	5.0000e+4	T_{tr}		Gokcen [50]
47	$H + e^- \leftrightarrow H+ + e^- + e^-$	2.20e+30	-2.80	1.5780e+5	T_{ve}		Park [28]

and *accurate* simulations of shock layer radiative heating, which make it ideal for coupled radiation and ablation simulations. The accuracy of HARA is achieved through its comprehensive set of radiation properties, including spectral data and non-Boltzmann models for diatomic molecules and atomic species, which were critically assessed and chosen in studies by Johnston et al. for air species [53, 54], ablation products [55], and Mars/Venus [47] species. Further details regarding HARA are provided by Johnston et al. [30].

3.3 Governing Surface Equations

Two of the primary governing surface equations that influence a coupled ablation solution are the surface energy balance and the species mass balance. The surface energy balance at the surface of a charring ablator is written as

$$q_c + \alpha q_{rad} - \epsilon\sigma {T_w}^4 - \dot{m}_c(h_w - h_c) - \dot{m}_g(h_w - h_g) - q_{cond} = 0 \tag{1}$$

The first two terms are the convective and absorbed radiative heating, which are a function of the flight condition, vehicle geometry, wall temperature, and injection of ablation products. The third term is the re-radiation from the ablator surface, which is a function of only the wall temperature and surface emissivity. The fourth and fifth terms are the enthalpy of injected char and pyrolysis gas, respectively. While h_w is the enthalpy of the gas at the wall, which is computed from the species composition obtained from the species mass balance and surface temperature, the enthalpy of the solid char (h_c) and pyrolysis gas (h_g) are typically determined experimentally and provided in table or curve-fit form for a given ablator. Finally, the heat conducted into the surface, q_{cond}, represents the inability of the previous three terms from relieving the incoming convective and radiative heat fluxes. This term depends on the time history of the surface temperature and is obtained from a material response code [56, 57]. The approach applied to solve the surface energy equation is described by Johnston et al. [30].

For equilibrium ablation, the solution of the species mass balance at the surface reduces to solving for the elemental mass balance. The solution to this problem is described by Johnston et al. [30]. The present work removes the equilibrium chemistry constraint at the surface by treating the individual finite-rate surface reactions, which provide the individual species mass fluxes due to surface reactions($\dot{m}_{c,i}$) [58]. Expressions for $\dot{m}_{c,i}$ are provided in the next subsection. With these expressions, the species mass balance at the surface is written as:

$$J_i + \left(\sum_j \dot{m}_{c,j} + \dot{m}_g \right) c_{w,i} - \dot{m}_{c,i} - \dot{m}_g c_{g,i} = 0 \tag{2}$$

where $\dot{m}_g$ represents the pyrolysis rate and $c_{g,i}$ are the species composition of the pyrolysis gases. The $c_{g,i}$ values are computed assuming chemical equilibrium, for the given elemental composition of the pyrolysis gas, at the surface temperature and pressure.

3.4 Finite-Rate Surface Chemistry Model

Recent advancements in finite-rate surface recession models provide the opportunity for enhanced simulation fidelity of an ablating heatshield's aerothermodynamic environment. Application of a finite-rate surface recession model, instead of an equilibrium ablation model, allows processes such as oxidation, sublimation, and surface catalysis to be modeled in detail, instead of relying on the assumption of chemical equilibrium at the surface elemental composition and temperature. The rate model compiled for this work, and presented in the following subsections, is based on values proposed by Park et al. [28] and Driver and Maclean [26], with additional sublimation reactions proposed by Keenan and Candler [59]. The choice of these rates is intended to provide a

model that is applicable over a wide range of conditions, ranging from the low-temperature rate-limited regime to the high-temperature sublimation regime.

3.4.1 Oxidation

The forward rate for the primary carbon oxidation reaction, O + C(s)→CO, is written as:

$$k_{f,O} = \gamma_O \sqrt{\frac{RT}{2\pi M_O}} \tag{3}$$

where $\gamma_O = 0.63e^{-1160/T}$ as suggested by Park et al. [28]. For the secondary oxidation reaction, O_2 + 2C(s)→2CO, the forward rate is written as:

$$k_{f,O2} = \gamma_{O2} \sqrt{\frac{RT}{2\pi M_{O2}}} \tag{4}$$

where $\gamma_O = (1.43 \times 10^{-3} + 0.01e^{-1450/T})/(1 + 2.0 \times 10^{-4} e^{13000/T})$ as proposed by Park et al [28]. Note that the temperature dependence of this term results in rate-limited oxidation at low temperatures, whereas if a constant is applied, such as the value of 0.01 suggested by Driver and Maclean [26], significantly larger oxidation values are obtained at low temperatures. The resulting species mass fluxes (kg/m^2/s) resulting from these processes are written as follows:

$$\dot{m}_{CO} = \frac{M_{CO}}{M_O} k_{f,O} \rho_O + 2 \frac{M_{CO}}{M_{O2}} k_{f,O2} \rho_{O2} \tag{5}$$

$$\dot{m}_O = -k_{f,O} \rho_O \tag{6}$$

$$\dot{m}_{O2} = -k_{f,O2} \rho_{O2} \tag{7}$$

where ρ_i are the species densities (kg/m^3) and M_i are the species molecular weights (kg/mol).

3.4.2 Sublimation

To accommodate the surface temperatures of up to 4000 K that may be encountered at Mars-return conditions, sublimation of C, C_2, C_3, and C_5 are treated similarly to Keenan and Candler [59]. The rate of sublimation for these molecules, expressed as xC(s)→C_x, are written as

$$\dot{m}_{C_x} = \alpha_{C_x} \left(\rho_{E,C_x} - \rho_{C_x} \right) \sqrt{\frac{RT}{2\pi M_{C_x}}} \tag{8}$$

where $\rho_{E,C_x} = A_x \, T^{n_x} \exp(-E_x/T)$ is the equilibrium vapor pressure (N/m^2). The coefficients for ρ_{E,C_x} are computed from Gordon and McBride [35] data and are listed in Table 3. The α_{C_x} values are taken from Keenan and Candler [59].

Table 3: Coefficients for sublimation rate equations.

C_x	α_x	A_x	n_x	E_x
C	0.14	1.486e+12	-1.487	87,110
C_2	0.26	1.8399e+17	-2.318	101,715
C_3	0.03	4.3197e+22	-3.459	103,339
C_5	0.015	2.6559e+15	-1.266	117,049

3.4.3 Nitridation and N_2 Recombination

The rate of nitridation, N + C(s)→CN, is written as

$$k_{f,N} = \gamma_N \sqrt{\frac{RT}{2\pi M_N}} \tag{9}$$

where the value of γ_N is set to 0.001 as derived by Driver and Maclean [26], which is significantly smaller than the 0.3 value proposed by Park et al [28]. For the N_2 recombination process, N + N(s)→N_2, the forward rate is written as:

$$k_{f,Nr} = \gamma_{Nr} \sqrt{\frac{RT}{2\pi M_N}} \tag{10}$$

where the value of γ_{Nr} is set to 0.05 as derived by Driver and Maclean [26].

$$\dot{m}_{CN} = \frac{M_{CN}}{M_N} k_{f,N} \rho_N \tag{11}$$

$$\dot{m}_N = -(k_{f,N} + k_{f,Nr}) \rho_N \tag{12}$$

$$\dot{m}_{N2} = k_{f,Nr} \rho_N \tag{13}$$

4.0 DIFFERENCES BETWEEN FINITE-RATE AND EQUILIBRIUM ABLATION

The forebody geometry considered in this section consists of a 60-degree sphere-cone with a nose radius of 0.45 m, shoulder radius of 0.033 m, and maximum diameter of 1.2 m. To capture the potential peak heating conditions for sample return mission, free-stream conditions with a density of 2e-4 kg/m^3 and velocities of 10, 12, and 14 km/s are considered. To simplify the comparison between the finite-rate and equilibrium ablation results, the wall temperatures are fixed for each case to the values presented in Fig. 1, which removes the need to solve the surface energy equation, and the ablator is assumed to be solid carbon with no pyrolysis, which simplifies the gas chemistry.

For the 14 km/s case, Fig. 2(a) compares the total surface mass flux, which is equal to the char rate as there is no pyrolysis, predicted by the equilibrium and finite rate surface models. The larger char rate predicted by the equilibrium model is seen in Fig. 2(b) to result, as expected, in a lower convective heating than the finite-rate model, while the radiative heating is nearly identical, which indicates that ablation has a negligible impact on ablation at these conditions.

To examine the difference between the char rates predicted by the two models, Figs. 2(c) and 2(d) present the individual species contributions to the surface mass flux, which is similar to the analysis performed by Candler [60]. For the finite-rate model, these values are obtained directly from Eqs. 3–13, while for the equilibrium model the surface mass flux from each is obtained from the species mass balance as follows

$$\dot{m}_i = J_i + (\dot{m}_c + \dot{m}_g)\, c_{w,i} - \dot{m}_g c_{g,i} \tag{14}$$

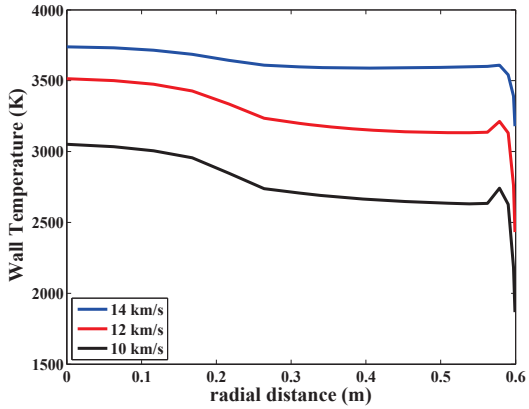

Figure 1: Fixed wall temperatures for comparisons between finite-rate and equilibrium ablation.

which reduces to the following for the present cases with no pyrolysis

$$\dot{m}_i = J_i + \dot{m}_c c_{w,i} \tag{15}$$

Note that in the solution procedure, the species mass balance is enforced indirectly through the elemental mass balance, which is the weighted sum of the species mass balance equations. In the elemental mass balance, the $\dot{m}_i$ term reduces to $\dot{m}_c \tilde{c}_{c,k}$, where $\tilde{c}_{c,k}$ is the given elemental composition of the char. Therefore, the $\dot{m}_i$ values computed in Eq. (15) are never actually used in the solution procedure, and are computed here as a post-processing step.

For the sublimation processes shown in Figure 2(c), it is seen that the finite-rate model predicts lower mass fluxes for C, C_3, and C_5, while it predicts higher mass fluxes for C_2. The corresponding species mass fractions through the stagnation line boundary layer are shown in Fig. 2(e).

Note that both the equilibrium and finite-rate models predict a significant negative mass flux for C. This negative mass flux implies that C is being re-deposited on the surface. If special treatment is not given to this negative flux, then it is being assumed that the re-deposited carbon forms a char of the same structure and density as the original char, and that this occurs directly on the surface. If this re-deposition actually occurs in-depth of a porous char, the negative mass flux of C would not be included in the total char rate at the surface, which would therefore result in an increased recession rate. However, this negative mass flux would be included in the in-depth material response density computation, which would change the in-depth char properties.

For species related to oxidation and nitridation, Figs. 2(d) and 2(f) present the mass fluxes and species mass fractions through the stagnation line boundary layer. The finite-rate model predicts small contributions from these processes, while the equilibrium model predicts moderate contributions from CN and N_2. The differences between the mass fraction profiles are primarily due to the differences in C_3, which alters the temperatures.

For the 12 km/s case, Fig. 3 presents the same comparisons as discussed previously for the 14 km/s case. Similarly to the 14 km/s case, the total surface mass flux in the stagnation region is seen in Fig. 3(a) to be significantly lower for the finite-rate case than the equilibrium case. Again, this is a consequence of the sublimation processes. Downstream of the stagnation region, however, Fig. 3(d) shows that the surface temperature decreases sufficiently for the oxidation processes to become dominant over the sublimation processes. Due to the diffusion-limited nature of the oxidation processes at these conditions, which makes them essentially independent of the oxidation rates or equilibrium ablation constraint, good agreement in the char rate is seen in

Fig. 3(a) along the conical region (>0.25 m) of the surface. Note that again, as discussed for the 14 km/s case, significant negative C mass flux is predicted by both the finite-rate and equilibrium models.

For the 10 km/s case, the temperatures in both the stagnation region and downstream are low enough for diffusion-limited oxidation to dominate. The resulting comparison between the finite-rate and equilibrium ablation models presented in Fig. 4 shows close agreement, with the main difference being the larger CN mass flux predicted by the equilibrium model. Again, a negative C mass flux is seen. Note that the negative O mass flux is a result of the oxidation process, and does not imply a net deposition of O on the surface.

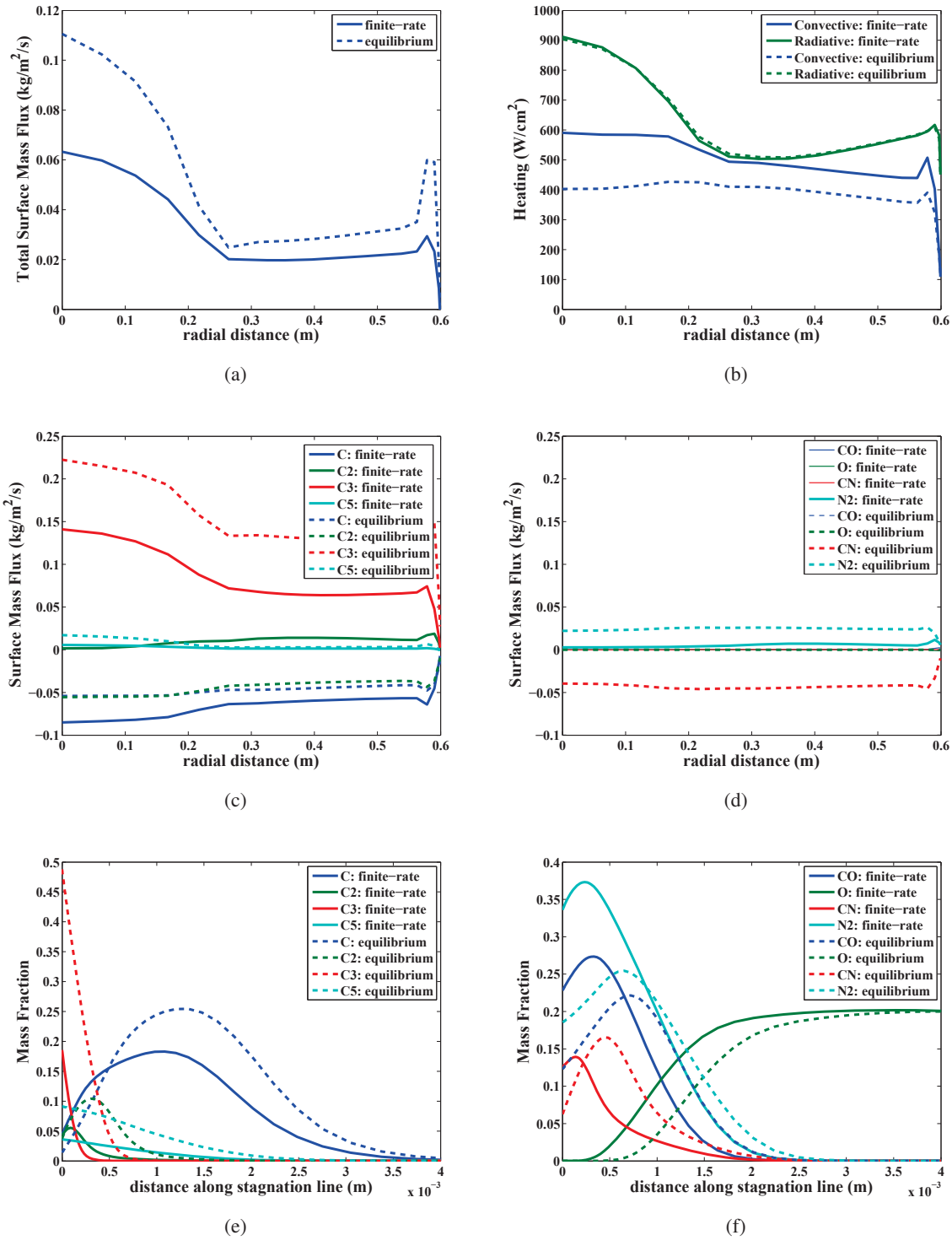

Figure 2: Comparison between surface mass flux, heating, and species profiles resulting from finite-rate and equilibrium ablation models for the 14 km/s case.

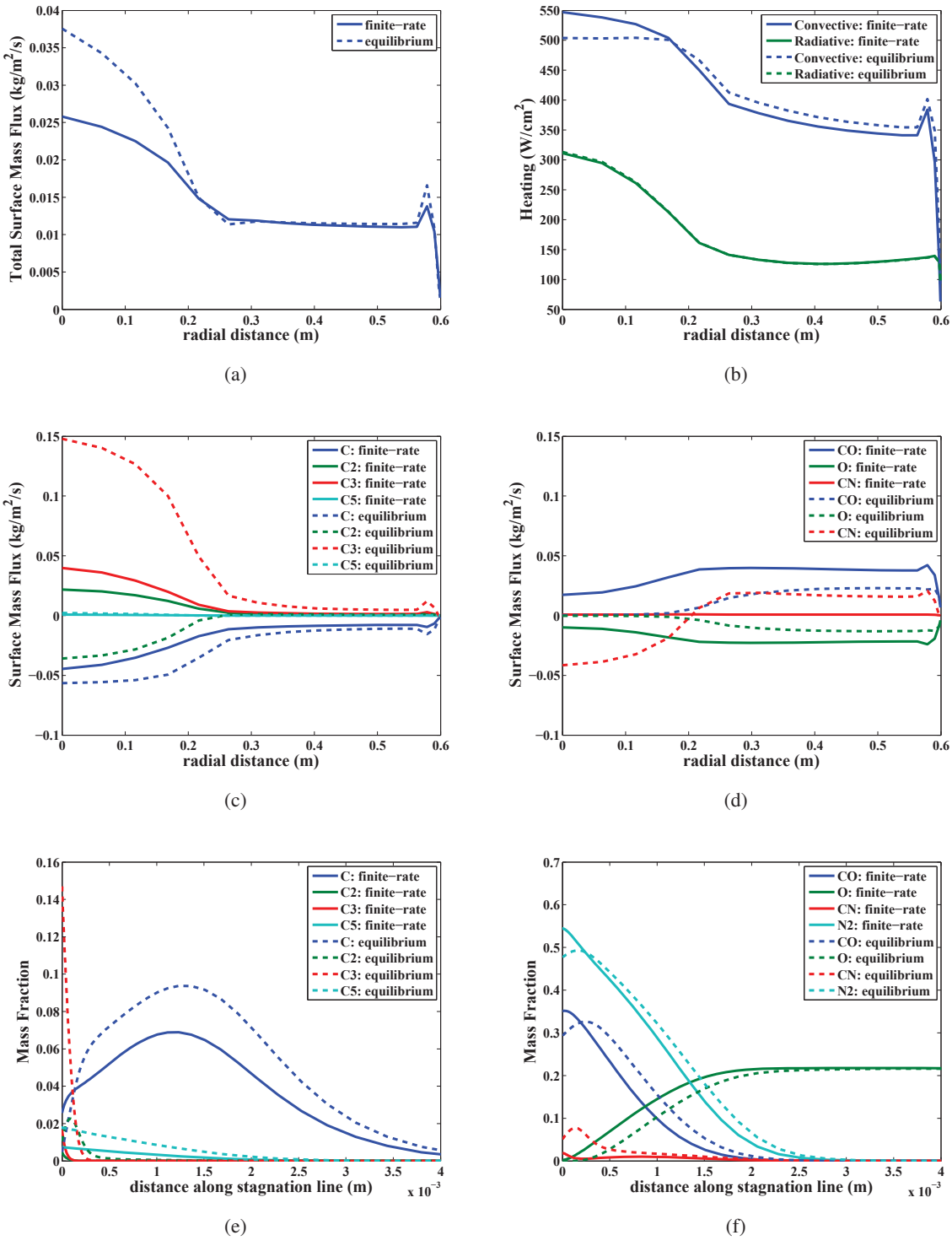

Figure 3: Comparison between surface mass flux, heating, and species profiles resulting from finite-rate and equilibrium ablation models for the 12 km/s case.

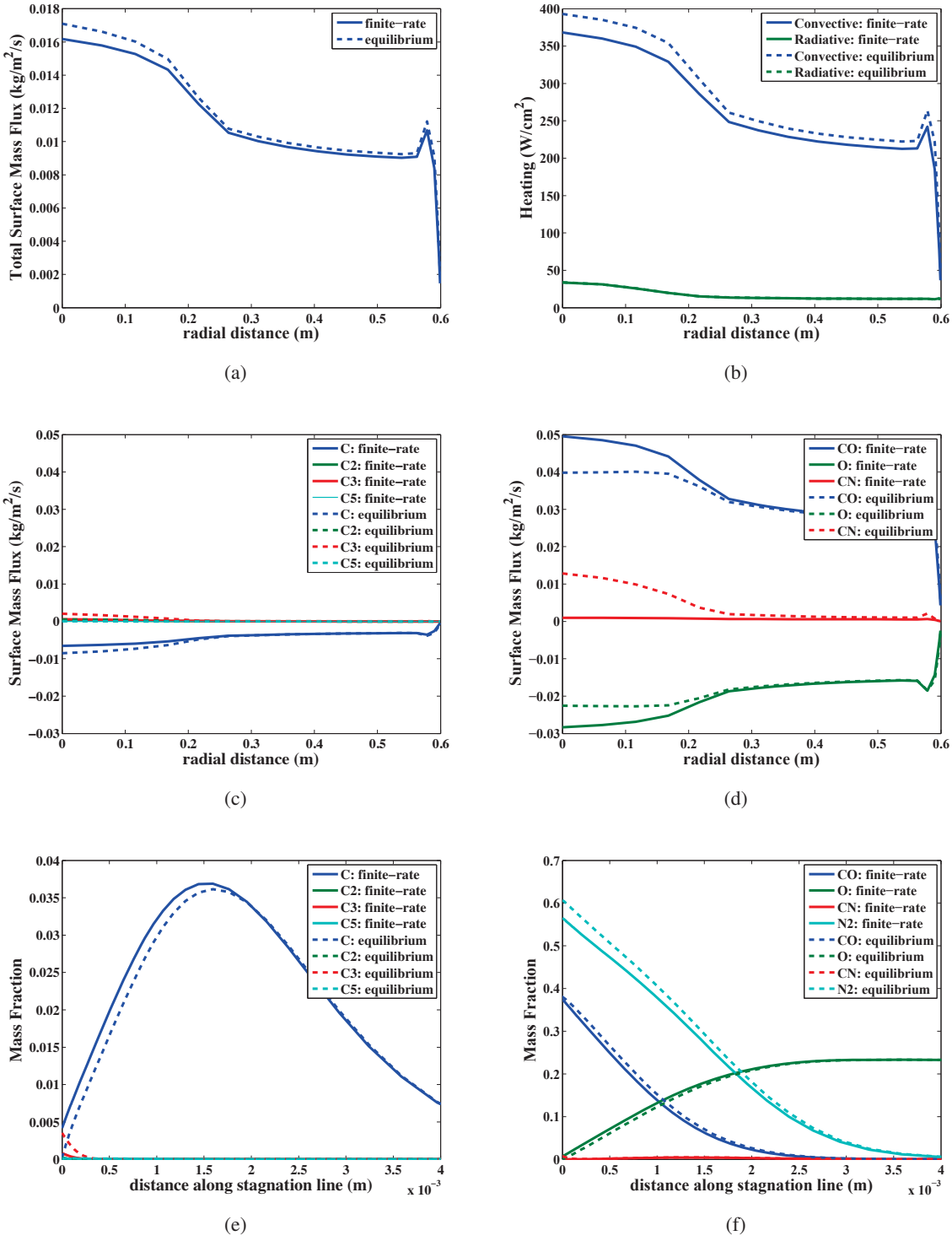

Figure 4: Comparison between surface mass flux, heating, and species profiles resulting from finite-rate and equilibrium ablation models for the 10 km/s case.

5.0 SENSITIVITY/UNCERTAINTY ANALYSIS FOR HIGH-SPEED SAMPLE-RETURN CASES

To assess the impact of flowfield and radiation modeling parameters on the convective heating, radiative heating, and char rate, sensitivity analyses were performed for the sample return cases considered in the previous section. The sensitivity to flowfield and radiation modeling parameters are treated separately, with the former in Section 5.1 and the latter in Section 5.2.

5.1 Flowfield Modeling Sensitivities

Rates for flowfield and surface chemistry are identified as the largest flowfield modeling contributors to the convective heating, radiative heating, and char rate uncertainties. To determine the most influential of these numerous rates, a sensitivity analysis was performed. This consisted of recomputing the coupled ablation-radiation flowfield with each flowfield rate increased and decreased by one order-of-magnitude and each surface rate increased and decreased by 1/2 order-of-magnitude. The magnitude of these one and 1/2 order-of-magnitude changes are chosen to approximate the possible uncertainty range for each rate. To simplify the analysis, the surface temperature is fixed for each case to the values presented in the previous section.

The resulting percent change in the stagnation-point convective heating, radiative heating, and char rate are presented in Table 4. Values resulting from an increased rate are listed first, while those resulting from a decreased rate are listed second in parenthesis. Only the 10 most influential flowfield rates are listed for clarity.

5.1.1 Impact on the Char Rate

It is instructive to consider first the impact of the rate changes on the char rate. The resulting changes in the computed char rate will influence strongly the convective and radiative heating, whereas because the surface temperature is fixed, the radiative and convective heating have no direct impact on the char rate. The impact of the flowfield rates (the first 10 rows in Table 4) provide limited influence for the 10 and 12 km/s cases, while for the 14 km/s case the dissociation rates are seen to cause changes of around 2% in the char rate. Not surprisingly, the impact of the surface rates (the last 8 rows in Table 4) on the char rates are seen to be considerable. These changes are also shown for each velocity in Fig. 5, which allows the differences away from the stagnation point to be seen.

Considering the 14 km/s case, Fig. 5(a) shows that the 1/2 order-of-magnitude increase in the C_3 sublimation rate results in a 41% increase in the total char rate at the stagnation point. This increased char rate improves the agreement with the equilibrium values presented in Fig. 2(a). Note that the C_3 mass fraction at the stagnation point is increased from 0.19 to 0.37 with this increase in the C_3 sublimation rate, while the equilibrium value is 0.49 (see Fig. 2(e)). Figure 5(a) also shows that a 1/2 order-of-magnitude increase in the C sublimation rate produces a decrease in the char rate. This decrease is a result of the negative contribution from C sublimation shown in Fig. 2(c).

For the 12 km/s case, Fig. 5(b) shows that changes in the sublimation rates influence the stagnation point, while downstream the influence is negligible. Unlike the 14 km/s case, changes in the C_3 and C rates provide char rate changes of similar magnitude. Figure 5(c) presents the results for the 10 km/s case, which is sensitive to only the oxidation rate. The diffusion-limited oxidation nature of the surface minimizes the influence of the 1/2 order-of-magnitude rate decrease to only a 7.7% decrease in the char rate.

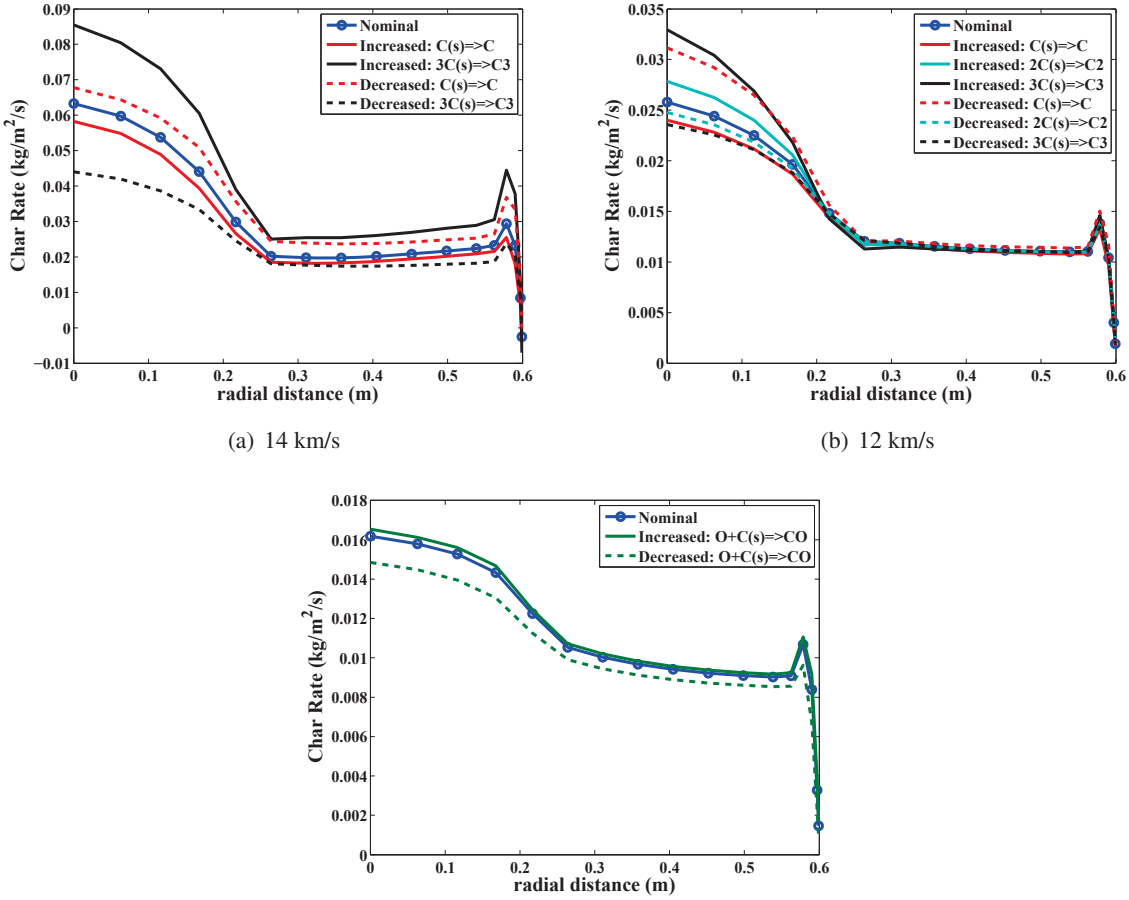

(a) 14 km/s

(b) 12 km/s

(c) 10 km/s

Figure 5: Sensitivity of the total char rate to 1/2 order-of-magnitude increases and decreases to individual surface rates.

Table 4: Sensitivities to one-order-of-magnitude change in the flowfield rates and 1/2-order-of-magnitude change in the surface rates. The result of the increased rate is listed first, while that from the decreased rate is listed in parenthesis. All values are in percent and those below 0.1% are replaced with a dash.

Parameter Group	Convective Flux			Radiative Flux			Char Rate		
	10 km/s	12 km/s	14 km/s	10 km/s	12 km/s	14 km/s	10 km/s	12 km/s	14 km/s
$N_2 + M \leftrightarrow N + N + M$	-	-	4.0(-0.8)	**-14.(5.2)**	-0.8(0.1)	-1.4(0.1)	-	-0.4(0.1)	-2.3(0.4)
$O_2 + M \leftrightarrow O + O + M$	-	-	-	-2.8(2.5)	-0.4(0.2)	-	-	-	-
$NO + M \leftrightarrow N + O + M$	-	-	3.5(-0.2)	**-9.1(20.)**	-1.0(3.9)	-1.7(-1.6)	-0.4(0.2)	-0.5(0.4)	-2.1(1.4)
$CO + M \leftrightarrow C + O + M$	-	-	4.0(-1.0)	-0.6(0.1)	-0.5(0.1)	-2.2(-0.7)	-	-0.3(0.1)	-2.4(0.6)
$N_2 + C \leftrightarrow CN + N$	0.1(-0.4)	1.2(-2.8)	-	-1.1(4.4)	-0.4(1.5)	-0.2(0.2)	0.2(-0.9)	-1.5(4.0)	-
$O_2 + N \leftrightarrow NO + O$	-	-	-	-0.8(0.4)	-0.3(0.3)	-	-	-	-
$CN + C \leftrightarrow C_2 + N$	-	-	-0.2(1.7)	-	-0.2(0.5)	-	-	1.8(-0.9)	0.3(-2.1)
$N + e^- \leftrightarrow N^+ + 2e^-$	-	-	-0.5(0.2)	2.5(-14.)	0.1(-0.3)	-0.9(0.4)	-	-	-0.5(0.1)
$O + e^- \leftrightarrow O^+ + 2e^-$	-	-	0.1(-1.3)	-1.9(1.1)	-1.3(2.8)	-0.8(-0.6)	-	-	-
$C + e^- \leftrightarrow C^+ + 2e^-$	-0.1(0.1)	0.8(-0.6)	3.3(-3.9)	1.8(-1.1)	-0.2(0.2)	-1.3(-2.2)	-	-0.8(0.6)	-1.0(2.3)
$O + C(s) \rightarrow CO$	-	-0.2(0.2)	-	0.4(-0.5)	-	-	2.8(-7.7)	1.5(-2.4)	-0.2(0.1)
$O_2 + 2C(s) \rightarrow 2CO$	-	-	-	-	-	-	-	-	-
$N + C(s) \rightarrow CN$	-	-	-	-	-	-	0.5(-0.2)	0.3(-0.1)	-
$C(s) \rightarrow C$	0.8(-2.1)	**4.5(-11.)**	**5.0(-12.)**	-	0.5(-1.2)	0.7(-1.8)	-1.8(4.1)	**-7.7(20.)**	**-4.1(12.)**
$2C(s) \rightarrow C_2$	-	-2.3(1.5)	-0.3(0.3)	-	-0.3(0.2)	-	0.3 (-0.2)	**7.0(-4.7)**	0.5(-0.4)
$3C(s) \rightarrow C_3$	-0.1(0.1)	**-7.3(2.3)**	**-20.(18.)**	-	-0.6(0.4)	-2.4(1.7)	0.6(-0.3)	**27.(-9.3)**	**41.(-28.)**
$5C(s) \rightarrow C_5$	-	-0.3(0.3)	-1.3(1.3)	-	-	-0.1(0.1)	-	1.4(-1.3)	4.0(-3.8)
$N + N(s) \rightarrow N_2$	**4.4(-9.0)**	2.0(-2.8)	-	-0.1(0.4)	-	-	0.7(-1.6)	0.3(-0.4)	0.3(-0.1)

5.1.2 Impact on the Convective Heating

Considering the convective heating, Table 4 shows that the flowfield rates (the first 10 rows) provide limited influence for the 10 and 12 km/s cases, while for the 14 km/s case the dissociation rates and electron-impact ionization of carbon are seen to contribute a more than 3% change in the convective heating. These changes are essentially due to changes in the char rate discussed above, and are therefore generally in the opposite direction of the char rate change (e.g. an increased char rate results in decreased convective heating). The impact of the surface chemistry on the convective heating is seen to be significantly greater, especially for the 14 km/s case, which sees a nearly $\pm 20\%$ change due to the C_3 sublimation rate. Again, this change is primarily due to the change in the char rate seen in the last column.

5.1.3 Impact on the Radiative Heating

The impact of the flowfield and surface rates on the radiative heating is seen to be relatively small for the 12 and 14 km/s cases, while the 10 km/s case sees a greater than 10% change due to the N_2 and NO dissociation rates. The large sensitivities are the result of strong nonequilibrium radiation from the NO band systems. Decreasing the dissociation rates increase the temperatures in the nonequilibrium region directly behind the shock, which causes an increase in the nonequilibrium emission. This influence is less for the 12 and 14 km/s cases because of their smaller nonequilibrium regions. The surface rate with the largest impact on the radiative heating is seen to be the C_3 sublimation rate, which causes a roughly 2% change for the 14 km/s case. This change is the result of increased absorption from C_3 due to the corresponding 41% increase in the char rate.

5.2 Radiation Modeling Uncertainty

Following the same approach as past studies by Johnston et al. [3] for computing the radiative heating uncertainty due to radiation modeling parameters, this section computes the uncertainty due to these parameters

Table 5: Summary of radiation modeling parametric uncertainties at the stagnation point. All values are percent and are the positive (+) uncertainty component.

Parameter Group	10 km/s	12 km/s	14 km/s
Air: Molec. Bands	3.20	2.74	2.20
Air: Atomic Lines: $f_{i,j}$	5.03	6.66	6.47
Air: Atomic Lines: $\Delta\lambda_{S,0}$	3.70	6.15	5.78
Air: Atomic Photoionization	2.80	4.63	4.57
Air: Opacity Project Lines	4.06	6.54	5.77
Air: Neg. Ion Photodetach.	1.38	0.88	0.62
AP: Molec. Bands	2.92	1.48	3.87
AP: Atomic Photoionization	0.83	1.17	2.56
Photo. Edge Shift	3.04	5.28	4.29
Total	27.0	35.5	36.1

instead of the sensitivity. This distinction between uncertainty and sensitivity is made because the uncertainty bounds of the radiation modeling parameters defined by Johnston et al. [3] are applied, instead of arbitrary values as done for the flowfield and surface rates discussed previously. Furthermore, the influence of the various radiation modeling parameters are essentially independent, which means the change in radiation due to each parameter may be added to obtain the total parametric uncertainty (assuming epistemic uncertainties). Note that the impact of the radiation modeling parameters on the convective heating and char rate, which occurs only through the radiation coupling, is negligible and therefore not considered.

The uncertainty values resulting from this analysis are presented in Table 5 for the stagnation point radiative heating. The individual components from the various radiative mechanisms are listed along with the total parametric uncertainty, which is the sum of the individual components. The rows in this table each refer to a specific group of the uncertainty parameters: "Air: Molec. Bands" and "AP: Molec. Bands" refer to the uncertainty resulting from Air and Ablation Product (AP) molecular band oscillator strength uncertainties; "Air: Atomic Lines: $f_{i,j}$" from all air atomic line oscillator strength uncertainties; "Atomic Lines: $\Delta\lambda_{S,0}$" from all air atomic line Stark broadening width uncertainties; "Air: Atomic Photoionization" and "AP: Atomic Photoionization" from all air and ablation product atomic photoionization cross section uncertainties; "Air: Opacity Project Lines" from all Opacity Project line uncertainties; "Air: Neg. Ion Photodetach." from all negative ion photodetachment cross section uncertainties. In addition to these uncertainties, the influence of the photoionization edge shift, which is not included in the baseline model, is listed in the "Photo. Edge Shift" row. This row represents simply the impact of adding these phenomena to the prediction. Similarly, the Opacity Project exclusive lines (meaning the lines that are included in the Opacity Project but not by NIST) are not included in the baseline radiation model. The "Air: Opacity Project Lines" row therefore represents the total contribution from these lines (it is always a positive contribution).

Table 5 shows that the radiative heating parametric uncertainty due to radiation modeling parameters ranges from 27% at 10 km/s to 36% at 14 km/s. Most of this uncertainty is due to air radiation, with ablation products contributing less than 7%. The top 10 individual contributors to the uncertainty are listed in Table 6. The top 3 contributors are seen to be bound-free cross sections of atomic carbon and nitrogen, which were each assigned an uncertainty of $\pm 20\%$. These cross-sections impact the boundary-layer absorption in the VUV region of the spectrum. The C_3 Swings, C_3 UV, and N_2 Birge-Hopfield I molecular band systems also appear on this list because of strong boundary layer absorption.

Table 6: Top uncertainty contributions from individual parameters for the 14 km/s case.

Rank	Parameter	Uncertainty ($\pm\%$)	$\pm q_{rad}$ (%)
1	σ_{bf} (C, level 1)	20	2.56
2	σ_{bf} (N, level 3)	20	1.42
3	σ_{bf} (N, level 2)	20	1.20
4	C_3 Swings	$O(1)$ mag.	0.88
5	$\Delta\lambda_{S,0}$ (N) – 174.4 nm	50	0.85
6	N_2 Birge-Hopfield I	50	0.64
7	C_3 UV	$O(1)$ mag.	0.62
8	σ^- (N^-)	100	0.62
9	f_{ij} (N) – 122.5 nm	75	0.57
10	$\Delta\lambda_{S,0}$ (N) – 122.5nm	75	0.36

5.3 Summary of Sensitivity/Uncertainty Analysis

A significant conclusion of this section is that, at 12 and 14 km/s, the char rate changes by 20-40% due to 1/2 order-of-magnitude changes in the sublimation rates for C_3 and C. If $\pm$1/2 order-of-magnitude represents a legitimate uncertainty bound for these rates (this assessment requires further study and is beyond the scope of this work), then the char rate uncertainty is greater than 20-40% at 12 to 14 km/s. Another notable conclusion is that the impact of flowfield chemistry is relatively small, and is overshadowed by the impact of surface rates.

Finally, the radiative heating uncertainty due to radiation modeling parameters ranges from 27 - 36% for the velocity range of 10 - 14 km/s. Because the impact of flowfield and surface rates on the radiative heating is less than 15% for the 10 km/s case, and less than 5% for the 12 and 14 km/s cases, the total radiative heating parametric uncertainty may be defined as the sum of the flowfield and radiation modeling parameter contributions, which results in a value of roughly 40% for each case.

6.0 COUPLED ABLATION AND RADIATION ANALYSIS OF STARDUST ENTRY

As discussed in Section 2, the final recession data and inferred surface temperature measurements make the Stardust entry an excellent test case for assessing a coupled ablation and radiation analysis. In this section, the coupled ablation and radiation approach discussed in Section 3 is applied to the Stardust trajectory listed by Trumble [14]. The forebody of the Stardust capsule consists of a 60-degree sphere-cone with a nose radius of 0.23 m, shoulder radius of 0.019 m, and maximum diameter of 0.81 m. The elemental composition of the pyrolysis gas from the PICA heatshield is taken from Park [61], while the char is assumed to be solid carbon with species mass fluxes obtained from the finite-rate model. The species and flowfield rates presented in Section 3 are applied.

6.1 Analysis Throughout the Trajectory

Figures 6 and 7 present the resulting convective and radiative heating, surface mass fluxes, contributions to the char rate from individual surface processes, and surface temperatures for the stagnation point and a downstream point at 0.25 m. These points were chosen because they approximate the locations where recession measurements were made. Note that the same vertical scale is applied to figures for both surface points to ease comparisons between the points.

For the heating shown in (a) of both figures, the convective heating is seen to dominate the radiative heating throughout the entire trajectory. While the impact of ablation on the radiative heating is negligible for these

cases, the convective heating is reduced significantly. For example, the stagnation point convective heating at t= 51 s is reduced by 30%, while the 0.25 m location is reduced by 11%.

For the char and pyrolysis rates presented in (b) of both figures, the result of equilibrium ablation, which was obtained using the pyrolysis rates and surface temperatures from finite-rate surface solution, is presented for comparison. Note that below t = 40 s, an equilibrium ablation solution was not obtainable because of convergence issues. The contributions to the char rate from the various surface processes are presented in (c) of both figures. The primary conclusion from these figures is that the finite-rate model matches the equilibrium model relatively closely in regions where diffusion-limited oxidation is dominant, identified in (c) between 70 - 80 s for the stagnation point and 42 - 75 s for the downstream point. Significant disagreement is seen where noticeable sublimation occurs, identified in (c) where the C_2 and C_3 components are noticeable, which is between 50 - 65 s for the stagnation point only, and where oxidation becomes rate controlled, identified in (c) where the O_2 oxidation component is noticeable, which is after 80 s for both points. These trends confirm the differences between finite-rate and equilibrium ablation discussed in Section 4.0.

The simulated temperature profiles presented in (d) of each figure are compared with the temperature inferred by Winter and Trumble [9] from the SLIT observation measurements. The stagnation point value is taken as the peak value defined by Winter and Trumble, while the value at 0.25 m is computed from their simplified temperature distribution. The good comparison between simulations and measurements is seen prior to 50 s, while from 50 s to the end of the measurement at 65 s an over-prediction of roughly 220 K is apparent. For the stagnation point, and to a lesser extent the downstream point, this over-prediction would be reduced with a larger sublimation rate in the finite-rate surface model. This larger rate would increase the char rate, which would decrease the convective heating and resulting surface temperature.

A comparison between the simulated final recession and the measured recession [62] from the recovered Stardust vehicle is presented in Fig. 8. As mentioned previously, the measurements were made near the stagnation point and near the radial location of 0.25 m. The present simulation is seen to under-predict the recession by 15% at the stagnation point and 20% at 0.25 m. Also presented for comparison are the uncoupled equilibrium ablation results of Stackpoole et al. [62], which are seen to over-predict by 61% at the stagnation point and 25% at 0.25 m. It is apparent that the present coupled finite-rate results present significantly better agreement at the stagnation point, and a similar magnitude of disagreement at 0.25 m. This result was anticipated by Beerman [63] using an uncoupled finite rate analysis. Note that the increase in the sublimation rate discussed in the previous paragraph would result in better agreement with the recession measurement at the stagnation point, although it is doubtful to have a noticeable impact at 0.25 m.

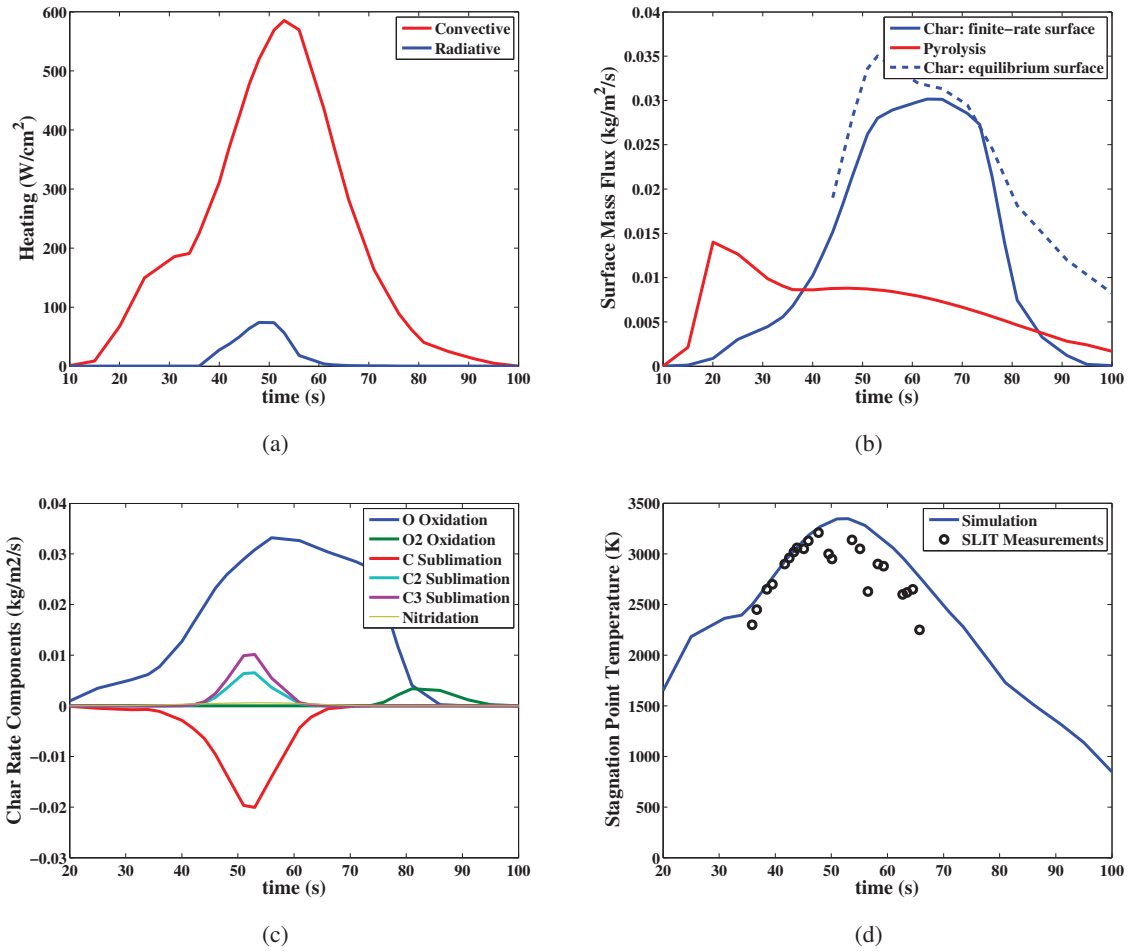

Figure 6: Stagnation point values from the Stardust coupled ablation and radiation analysis.

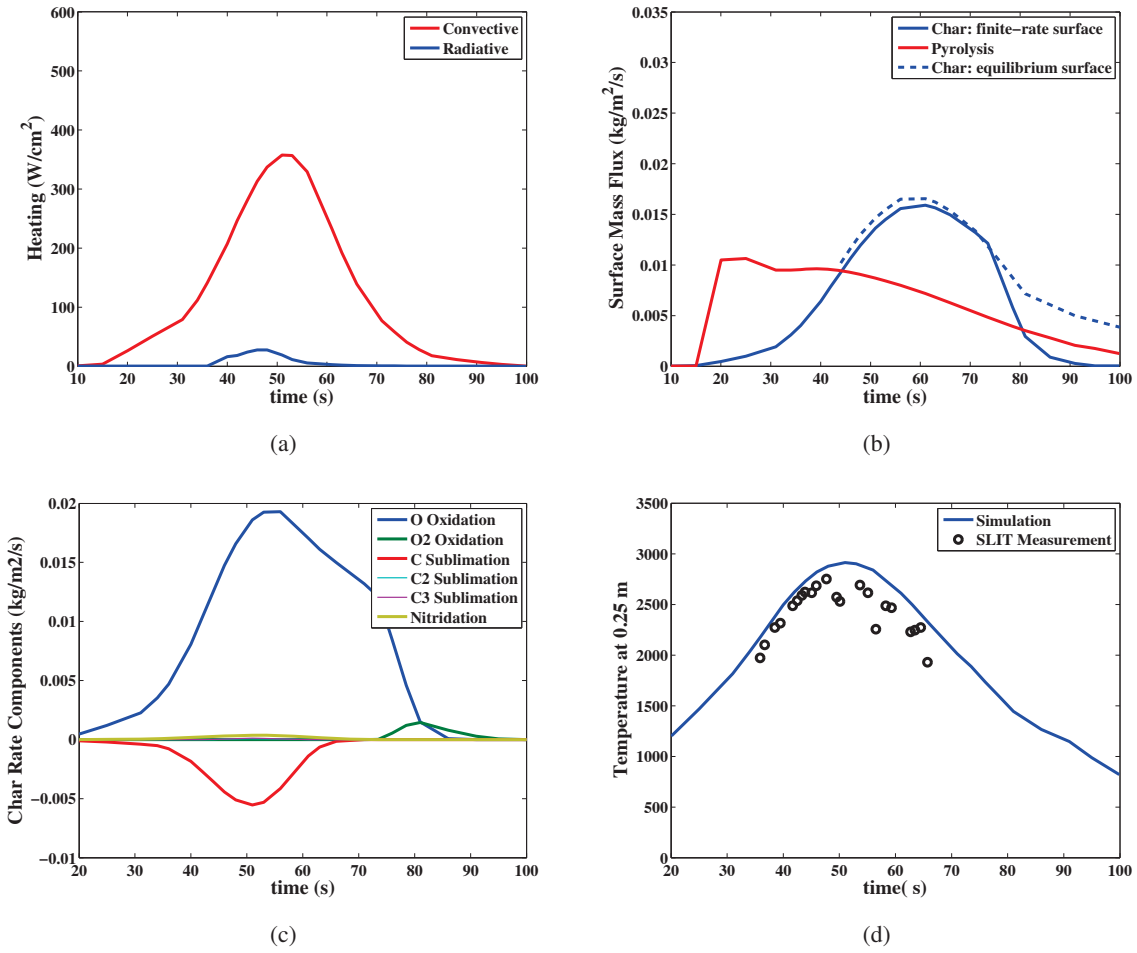

Figure 7: Values at a radial distance of 0.25 m resulting from the Stardust coupled ablation and radiation analysis.

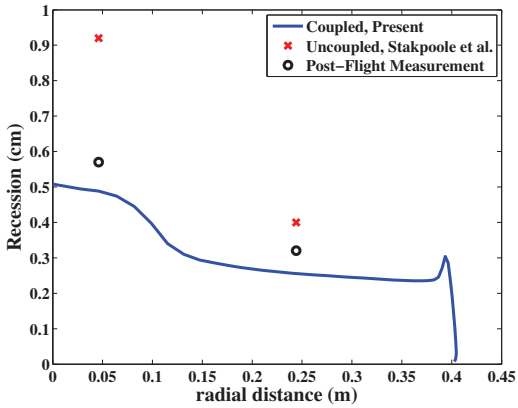

Figure 8: Final recession values for Stardust entry.

6.2 Detailed Analysis of Two Trajectory Points

To provide further insight into the influence of coupled ablation on the convective and radiative heating, trajectory points at t = 42 and 53 s are studied in detail. The 42 s point, which is at 12.06 km/s and 5.6e-5 kg/m^3, contains significant thermochemical nonequilibrium, while the 53 s point, which is at 10.42 km/s and 2.7e-4 kg/m^3, represents the peak heating point.

The primary surface values for the 42 s point are presented in Fig. 9. To show the impact of ablation, the heating and wall temperatures are compared with the non-ablating simulations. A significant reduction in both the surface temperature and convective heating is seen along the entire surface due to ablation. The radiative heating, however, is seen to increase by as much as 38%.

To explain this increased radiative heating, Fig. 10 presents relevant values along the stagnation line. For the number densities shown in (a), where only a subset of the species are shown for clarity, the air species are identified by solid lines and those resulting from ablation products are identified by dashed lines. Considering the temperatures shown in (a) and the number densities shown in (b), it is seen that many of the ablation products extend into regions with temperatures greater than 10,000 K. The consequence of this on the radiative emission is shown in (c), where CN Violet, CN Red, and CO 4th Positive are seen to emit strongly near the outer edge of the boundary layer. For the atomic species, which diffuse furthest into the shock layer, (d) shows that atomic line emission from C and H is on the same order as O throughout most of the shock layer. Finally, (e) and (f) compare the wall-directed radiative flux profile and spectrum for the coupled ablation and non-ablating case. In addition to the shock standoff being slightly larger for the ablation case, the emission from the ablation products seen in (c) and (d) are shown to increase the radiative flux. The ablation product radiation is apparent in (f) wherever the red spectrum is visible. The CN Violet band is seen around 3.2 eV and many atomic lines, resulting from C and H are seen from 5 to 10 eV.

Note that the impact of ablation shown here disagrees with the results of Alkandry et al. [64], who show that assuming an equilibrium pyrolysis gas results in a significant reduction in the convective heating and char rate relative to a frozen pyrolysis gas assumption. This result was not seen in the present work. To check if the additional species and rates applied by Alkandry et al. were responsible for this influence, the present case at 42 s was recomputed with the additional species and rates, and a negligible change in the char rate and convective heating was seen. It is therefore likely that this disagreement with Alkandry et al. is the result of different

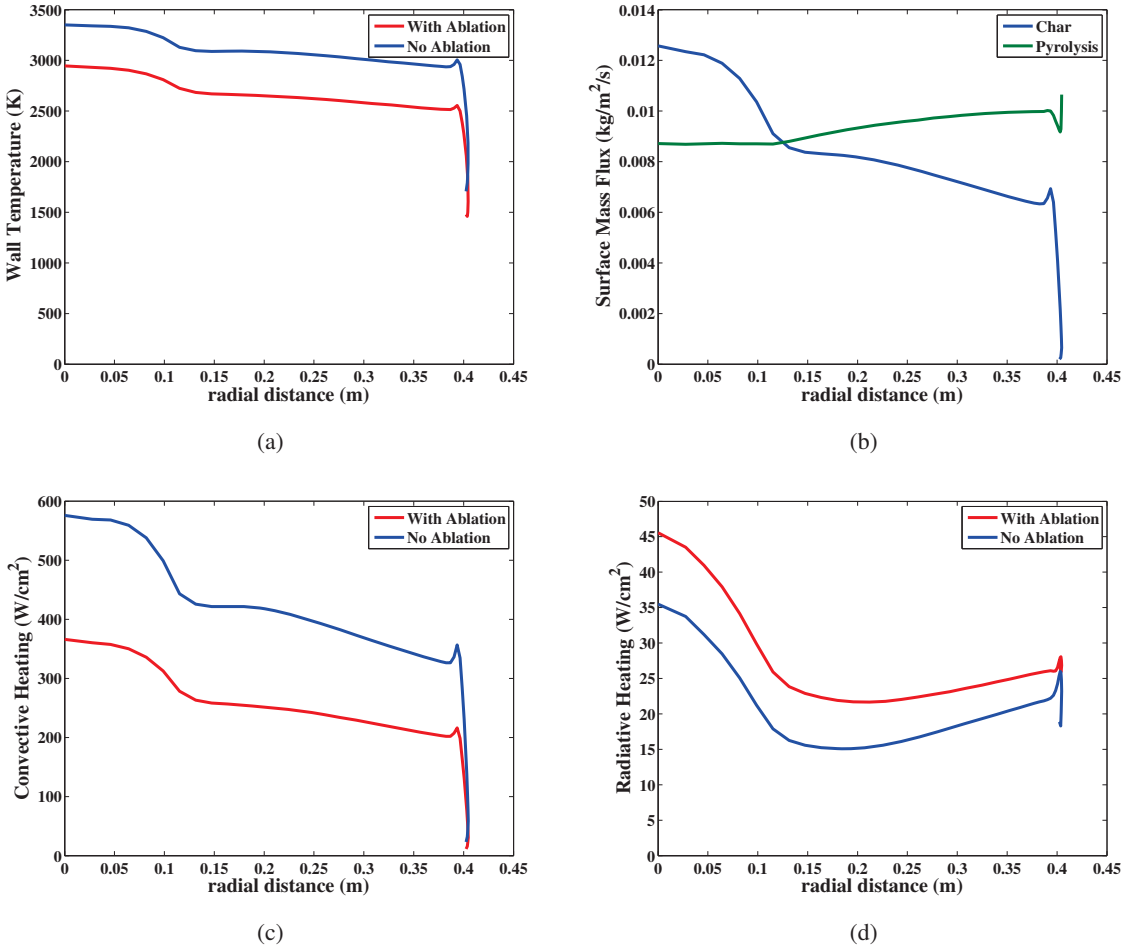

Figure 9: Surface values for the t = 42 s Stardust case.

ablation materials being studied, with TACOT considered by Alkandry et al. and PICA considered here. This argument is strengthened by considering the equilibrium composition of the pyrolysis gas, which is dominated by CO and H_2 in the present study, while significant C_2H_2 is reported by Alkandry et al.

For the t = 53 s case, Figs. 11 and 12 provide the same comparisons as presented for the 42 s case. Although the char rate is nearly double the 42 s value and the pyrolysis rates are similar, the impact of ablation on the convective and radiative heating is seen to be less for the 53 s case. This is the result of the non-dimensional ablation rate (equal to the char plus pyrolysis rate divided by the free-stream density and velocity) being smaller by nearly a third for 53 s case. Figure 12(c) and (d) show that the ablation products (CN, CO, C and H) provide a smaller contribution to the emission relative to the air species than was seen for the 42 s case.

6.3 Comparison with Observations

Regarding the vibrational and translational temperatures inferred at 42 s by Winter and Trumble [9] from CN Violet measurements, the peak CN Violet emission shown in Fig 10(c) occurs at 0.18 cm, which has a T_{ve} of 8820 K and T_{tr} of 8670 K. These temperatures are compared with the inferred values of 6000 K for the

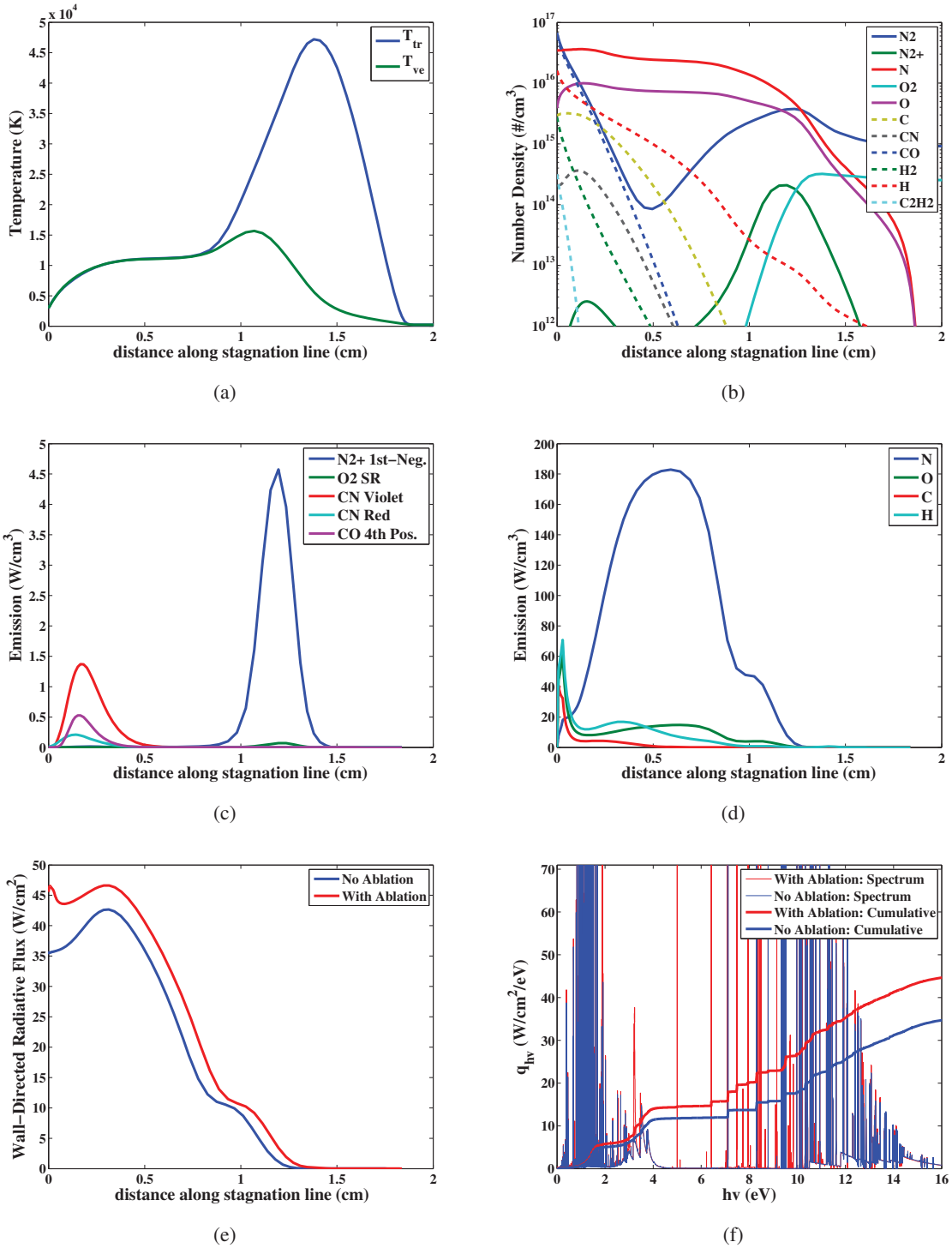

Figure 10: Stagnation-line values for the t = 42 s Stardust case.

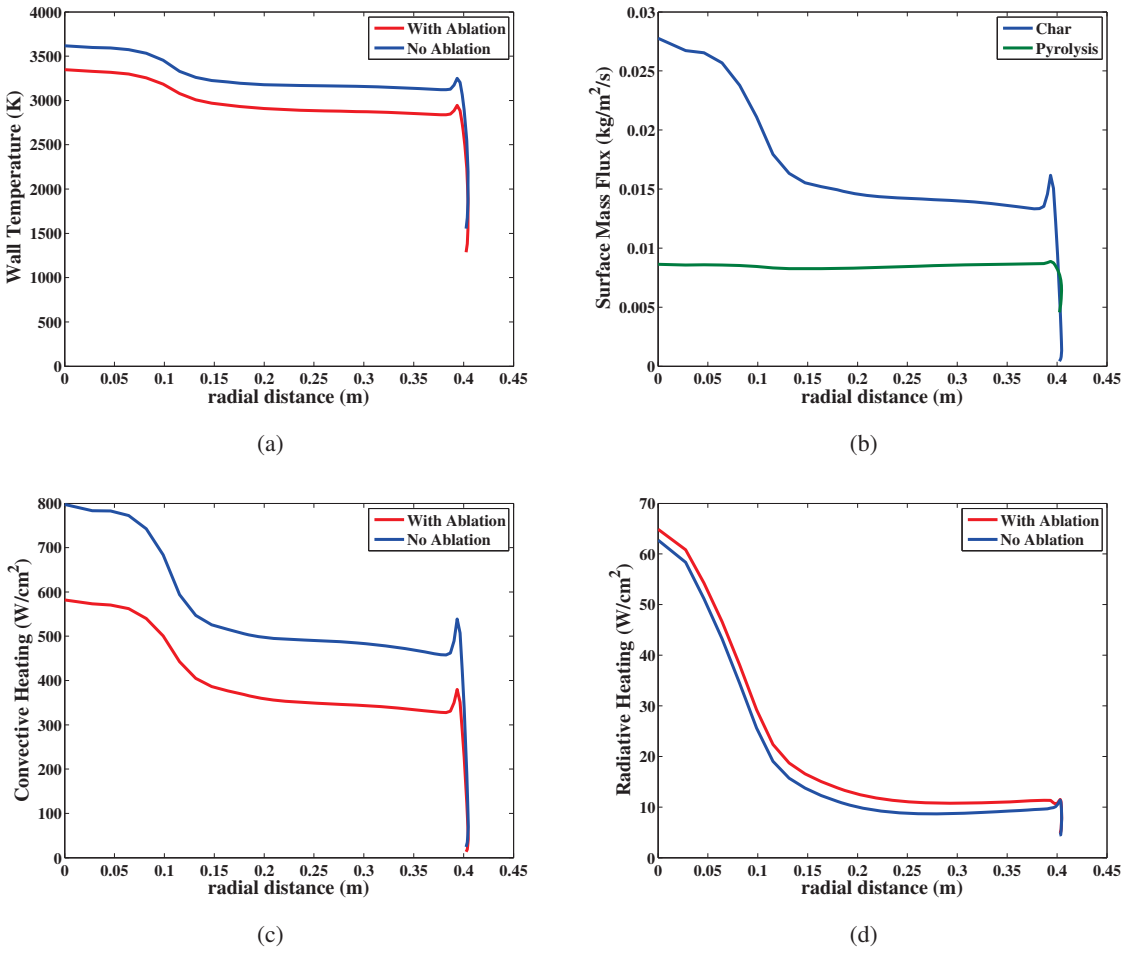

Figure 11: Surface values for the t = 53 s Stardust case.

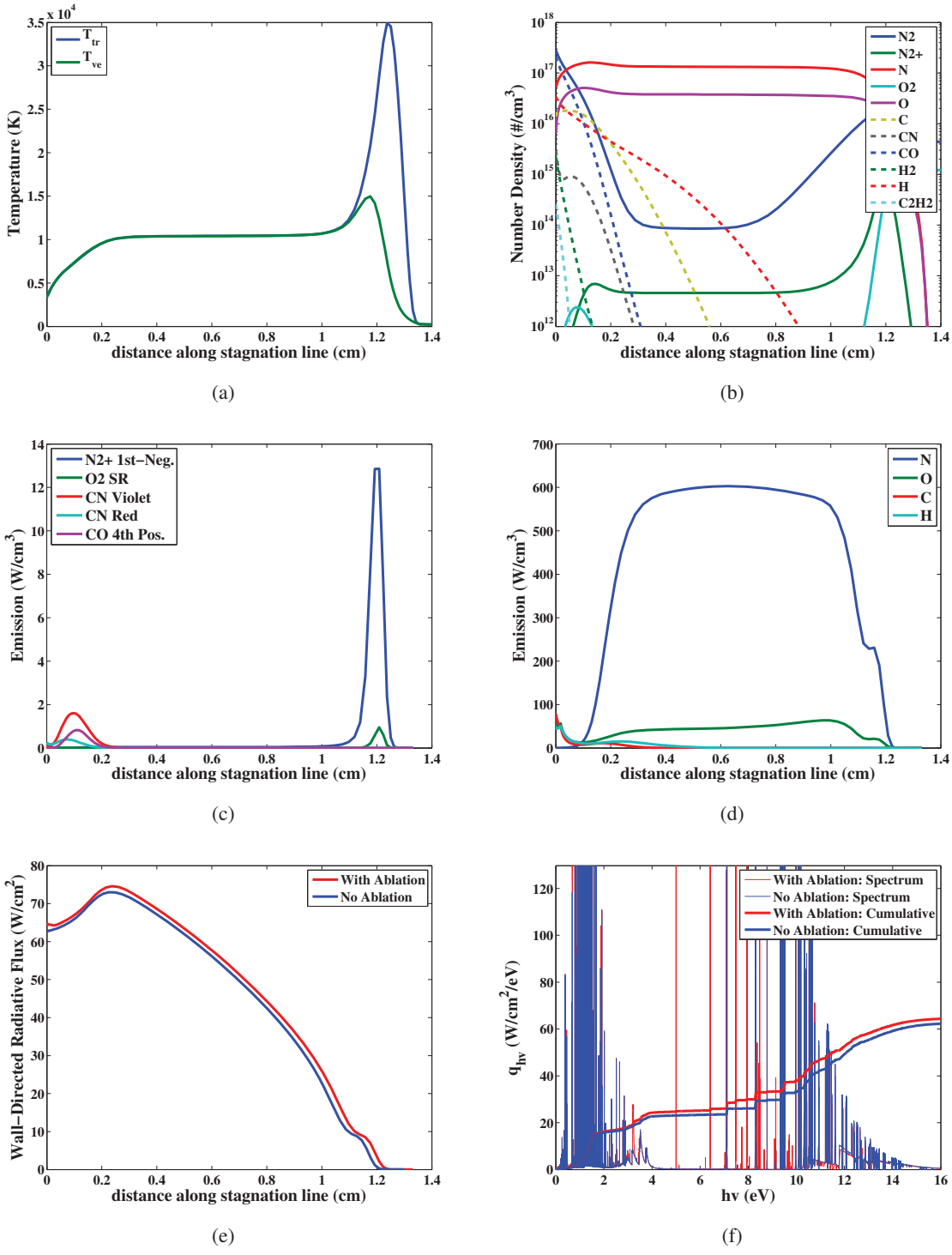

Figure 12: Stagnation-line values for the t = 53 s Stardust case.

rotational and 9000 K for the vibrational temperatures. The simulated and inferred values are close enough to conclude that the location throughout the shock layer of the CN Violet emission is simulated with decent accuracy, although the magnitude may not be predicted well.

A ray-tracing algorithm was applied to compute the observed spectrum measured by Winter and Trumble [9] and Jenniskens [10] using the present coupled solutions. For the 42 s point, Fig. 13 compares the Echelle measurement by Jenniskens [10], which provide similar values to the SLIT measurements for the CN Violet band [9], with the present simulations. A significant over-prediction of the CN Violet band is seen, which is consistent with the results seen by Martin and Boyd [65], obtained with different chemical rates and ablation models. As mentioned by Martin and Boyd, the rate $CO + N \leftrightarrow CN + O$ has a significant impact on this over-prediction, while it is also found that $CN + O \leftrightarrow NO + C$ has a significant impact. An order-of-magnitude decrease in the former and increase in the latter is found to reduce the simulated CN Violet flux by one half. Another possible source of disagreement is the non-Boltzmann model. The present model is predicting that the upper-state population of CN Violet is at 99% of its Boltzmann limit. Significant uncertainty exists for the non-Boltzmann rates, and different rates could potentially lead to lower populations and therefore lower emission. Note that in addition to showing disagreement for the CN Violet band, the band edge seen at 392 nm is from N_2^+ First-Negative, which is shown to also be significantly over-predicted. As seen in in Fig 10(c), this band system radiates strongest in the nonequilibrium post-shock region.

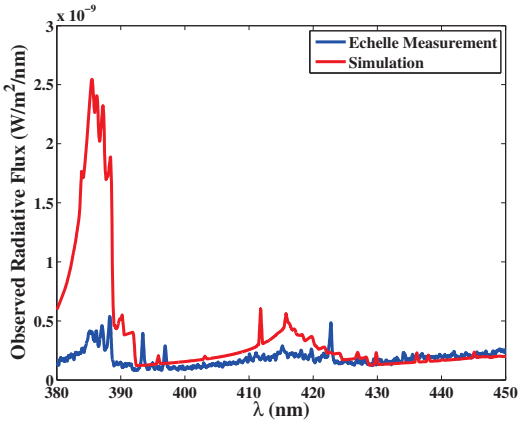

Figure 13: Comparison with Echelle measurements at t = 42 s.

7.0 COUPLED ANALYSIS OF A MARS SAMPLE RETURN CAPSULE

As a final example of the coupled ablation and radiation analysis developed in this work, an Earth entry trajectory representative of a 14 km/s Mars sample return is considered. The trajectory points considered in the present analysis are presented in Table 7. The forebody shape considered is the same as that treated in Sections 4.0 and 5.0, which is a 60-degree sphere-cone with a nose radius of 0.45 m, shoulder radius of 0.033 m, and maximum diameter of 1.2 m The same PICA ablation model applied in the previous Stardust analysis is applied here. Because of the larger nose radius and higher entry velocity than for Stardust, radiation will provide a larger fraction of the total heating.

Stagnation point values through the trajectory are presented in Fig. 14. Comparing these values to the stagnation point values for Stardust shown in Fig. 6, it is seen that, as expected because of the larger nose radius

Table 7: Free-stream conditions for a high-speed Earth entry representative of a Mars sample return.

t (s)	U_∞ (km/s)	ρ_∞ (kg/m^3)
12	14.00	2.60e-6
13	14.74	4.20e-6
14	13.97	6.72e-6
16	13.89	1.57e-5
18	13.72	3.47e-5
20	13.36	7.17e-5
21	12.89	1.17e-4
23	12.22	1.82e-4
25	10.98	3.05e-4
27	9.43	4.71e-4
29	7.81	6.70e-4
32	5.66	1.01e-3
35	4.06	1.38e-3
38	2.96	1.78e-3
41	2.22	2.18e-3

and faster entry velocity for the present case, the radiative heating is significantly larger while the convective heating is lower. Furthermore, (c) of this figure shows that sublimation contributes significantly around peak heating.

The peak heating point for this trajectory occurs at 23 s, which has free-stream conditions close to those for the 12 km/s example studied in Sections 4 and 5. Surface values for the 23 s point are presented in Fig. 15, while stagnation line values are presented in Fig. 16. Other than the radiative heating and sublimation being larger, these figures are similar to those in Fig. 11 and 12 for the Stardust peak heating at 53 s. It is seen in (b) that the C_2 and C_3 resulting from sublimation are restricted to a narrow region near the surface. This explains why significant absorption from the C_3 Swings band system is not seen.

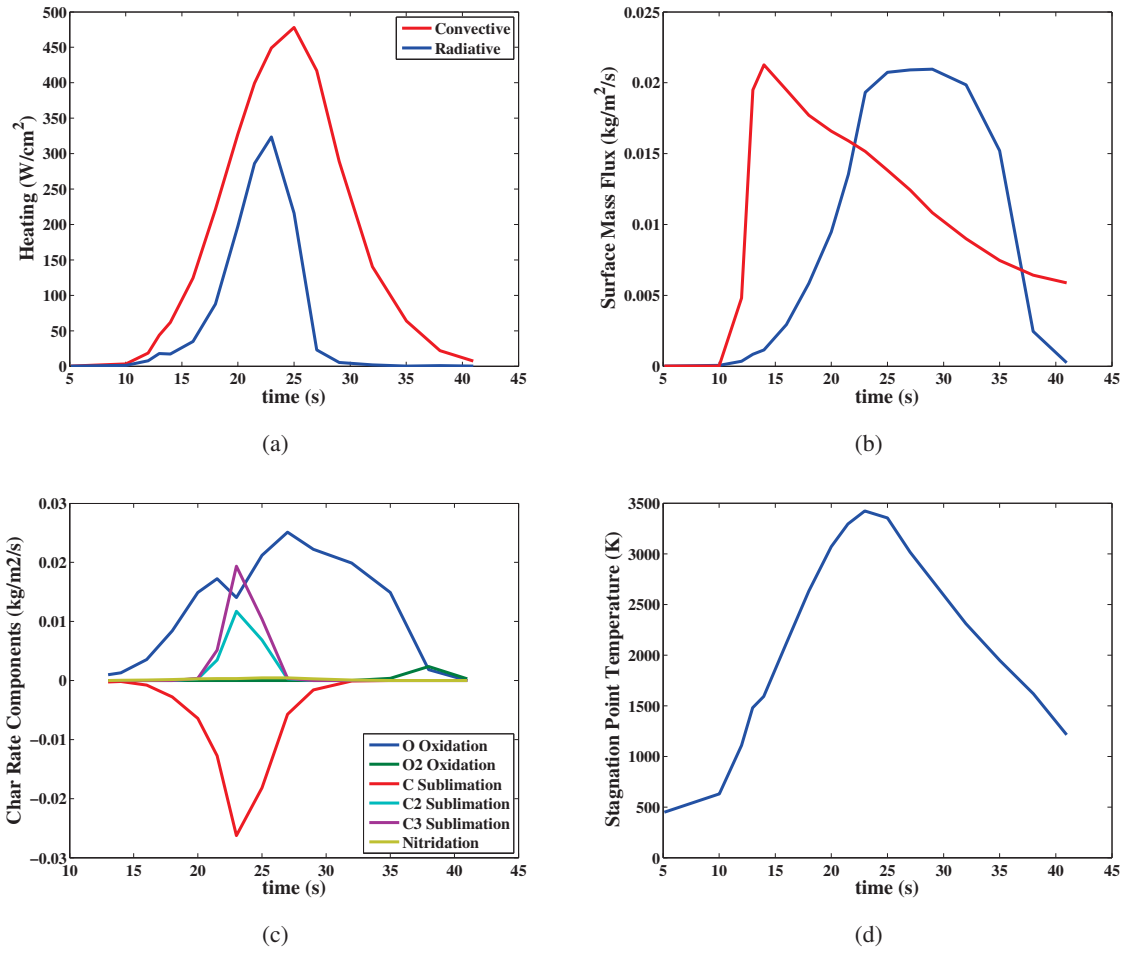

Figure 14: Stagnation point values from the Mars sample return coupled ablation and radiation analysis.

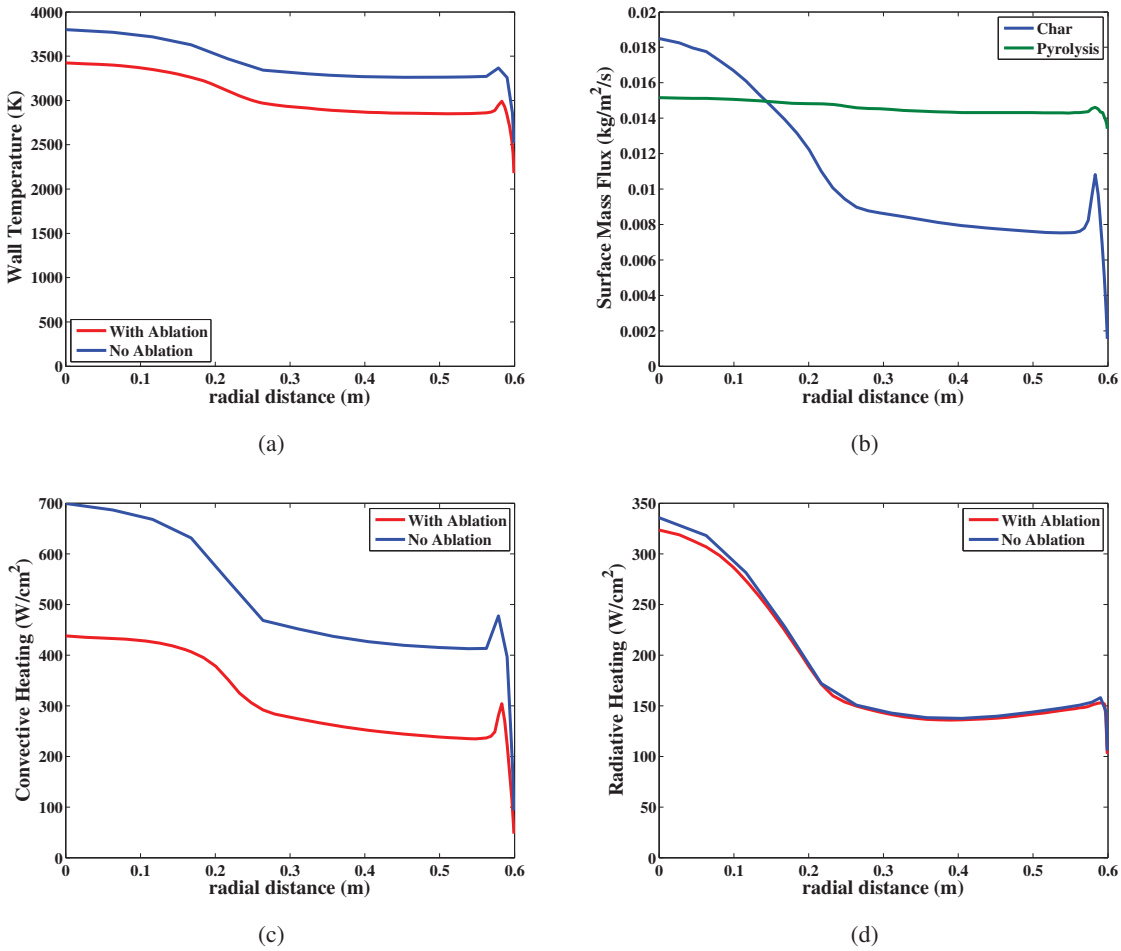

Figure 15: Surface values for the t = 23 s Mars sample return case.

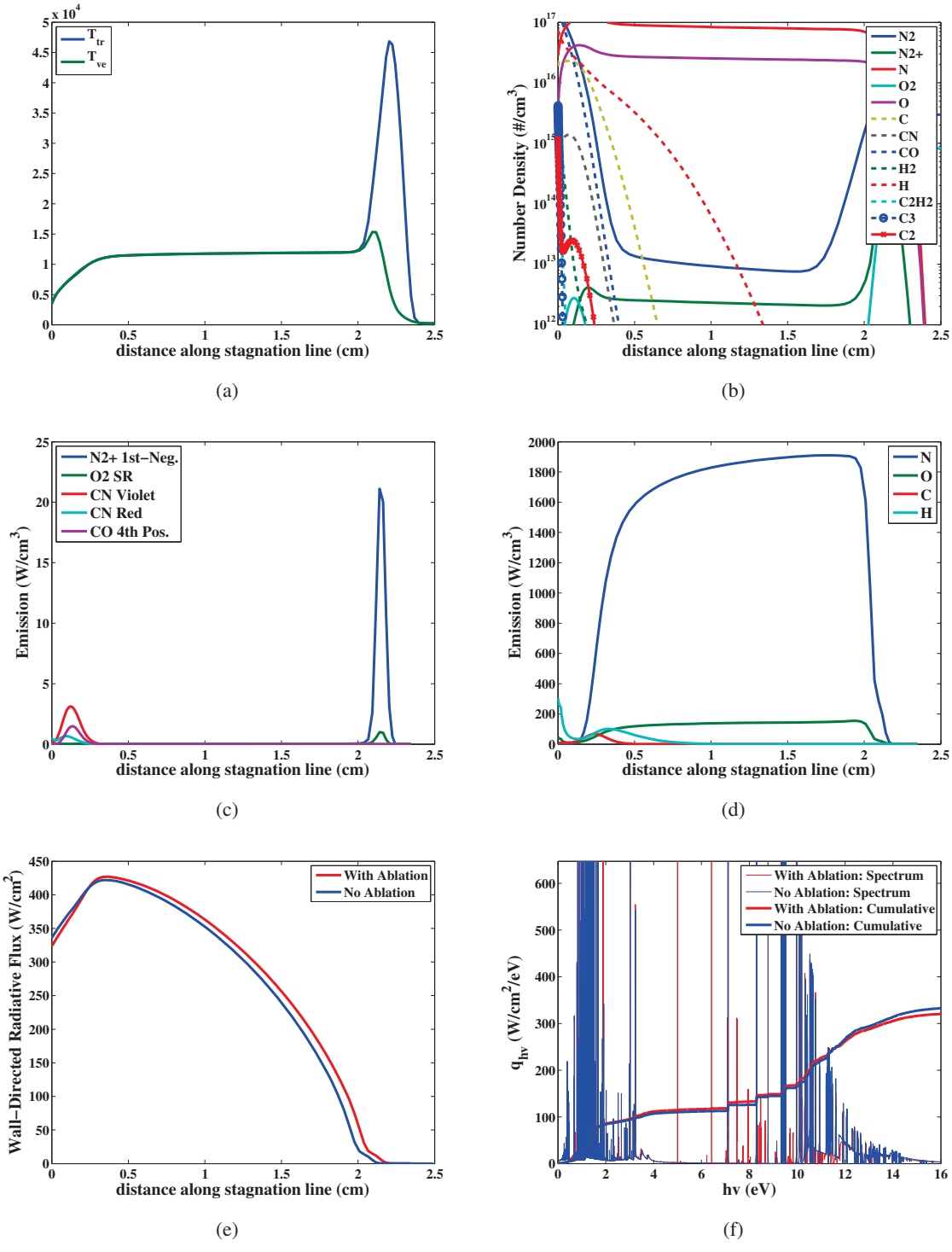

Figure 16: Stagnation-line values for the t = 23 s Mars sample return case.

REFERENCES

[1] Tsou, P., Brownlee, D. E., McKay, C. P., Anbar, A. D., Yano, H., Altwegg, K., Beegle, L. W., Dissly, R., Strange, N. J., and Kanik, I., "LIFE: Life Investigation For Enceladus A Sample Return Mission Concept in Search for Evidence of Life," *Astrobiology*, Vol. 12, No. 8, pp. 240–249.

[2] Tito, D., Carrico, T. M. J., and Loucks, M., "Feasibility Analysis for a Manned Mars Free-Return Mission in 2018," Aiaa keynote speech, 2013.

[3] Johnston, C. O., Mazaheri, A., Gnoffo, P., Kleb, B., and Bose, D., "Radiative Heating Uncertainty for Hyperbolic Earth Entry, Part 1: Flight Simulation Modeling and Uncertainty," *Journal of Spacecraft & Rockets*, Vol. 50, No. 1, 2013, pp. 19–38.

[4] Johnston, C. O., Sutton, K., Prabhu, D., and Bose, D., "Radiative Heating Uncertainty for Hyperbolic Earth Entry, Part 2: Comparisons with 1960s Era Shock Tube Measurements," *Journal of Spacecraft & Rockets*, Vol. 50, No. 1, 2013, pp. 39–47.

[5] Johnston, C. O., Brandis, A. M., and Bose, D., "Radiative Heating Uncertainty for Hyperbolic Earth Entry, Part 3: Comparisons with EAST Measurements," *Journal of Spacecraft & Rockets*, Vol. 50, No. 1, 2013, pp. 48–55.

[6] Johnston, C. O. and Brandis, A. M., "Assessment of Afterbody Radiative Heating Simulation and Uncertainty for Earth Entry," AIAA Paper 2014–XXXX, 2014.

[7] Stackpoole, D. K. M., "Post-Flight Analysis of the Stardust Sample Return Capsule Earth Entry," AIAA Paper 2008–1197, 2008.

[8] Suzuki, T., Fujita, K., Yamada, T., Inatani, I., and Ishii, N., "Post-Flight TPS Analysis of Haybusa Reentry Capsule," AIAA Paper 2011–3759, 2011.

[9] Winter, M. and Trumble, K., "Near-Ultraviolet Emission Spectroscopy During an Airborne Observation of Stardust Reentry," *Journal of Spacecraft & Rockets*, Vol. 48, No. 1, 2011, pp. 59–71.

[10] Jenniskens, P., Koop, M., and Albers, J., "Intensified Low-Resolution Optical Spectroscopy of the Stardust Sample Return Capsule Entry," *Journal of Spacecraft & Rockets*, Vol. 47, No. 6, 2010, pp. 895–900.

[11] Jenniskens, P., "Observations of the Stardust Sample Return Capsule Entry with a Slitless Echelle Spectrograph," *Journal of Spacecraft & Rockets*, Vol. 47, No. 5, 2010, pp. 718–735.

[12] Buttsworth, D., Morgan, R., and Jenniskens, P., "Near-Ultraviolet Emission Spectroscopy of the Hayabusa Reentry," *Journal of Spacecraft & Rockets*, Vol. 50, No. 6, 2013, pp. 1109–1120.

[13] Yamada, T., Inatani, Y., Ishii, N., Hirai, K., and Morita, S., "Reentry of Hayabusa Sample Return Capsule and Post-flight Analysis of Recovered Heatshield," AIAA Paper 2011–3322, 2011.

[14] Trumble, K. A., "Post-Flight Aerothermal Analysis of the Stardust Sample Return Capsule," *Journal of Spacecraft & Rockets*, Vol. 47, No. 5, 2010, pp. 765–774.

[15] Liu, Y., Prabhu, D., Trumble, K. A., Saunders, D., and Jenniskens, P., "Radiation Modeling for the Reentry of the Stardust Sample Return Capsule," *Journal of Spacecraft & Rockets*, Vol. 47, No. 5, 2010, pp. 741–752.

[16] Cauchon, D. L., "Radiative Heating Results from the Fire II Flight Experiment at a Reentry Velocity of 11.4 Kilometers Per Second," NASA TM X 1402, July 1967.

[17] Johnston, C. O., Hollis, B., and Sutton, K., "Nonequilibrium Stagnation-Line Radiative Heating for Fire II," *Journal of Spacecraft & Rockets*, Vol. 45, Nov.-Dec. 2008, pp. 1185–1195.

[18] Kleb, B., Thompson, R., and Johnston, C. O., "Blurring the Inputs: A Natural Language Approach to Sensitivity Analysis," AIAA Paper 2007–4206, June 2007.

[19] Palmer, G., "Uncertainty Analysis of CEV LEO and Lunar Return Entries," AIAA Paper 2007–4253, June 2007.

[20] Johnston, C. O. and Kleb, B., "Uncertainty Analysis of Air Radiation for Lunar-Return Shock Layers," *Journal of Spacecraft & Rockets*, Vol. 49, No. 3, 2012, pp. 425–434.

[21] Brandis, A. M., Johnston, C. O., Cruden, B. A., Prabhu, D. K., and Bose, D., "Validation of High Speed Earth Atmospheric Entry Radiative Heating from 9.5 to 15.5 km/s," AIAA Paper 2012–2865, 2012.

[22] Johnston, C. O., "A Comparison of EAST Shock Tube Radiation Measurements with a New Air Radiation Model," AIAA Paper 2008–1245, Jan. 2008.

[23] M. Panesi, T.E. Magin, A. B. A. B. and Chazot, O., "Collisional radiative modeling in flow simulation," VKI Lecture STO-AVT-162, 2008.

[24] Potter, D., "Modeling of Radiating Shock Layers for Atmospheric Entry at Earth and Mars," Ph.d. dissertation, 2011.

[25] Lemal, A., "Prediction of Nonequilibrium Air Radiation with a Collisional-Radiative Model: Application to Shock-Tube Experiments Relevant to Earth Atmospheric Reentry," Ph.d. dissertation, 2012.

[26] Driver, D. and MacLean, M., "Improved Predictions of PICA Recession in Arc Jet Shear Tests," AIAA Paper 2011–0141, 2011.

[27] Chen, Y. K. and Gocken, T., "Effect of Nonequilibrium Surface Thermochemistry in Simulation of Carbon-Based Ablators," *Journal of Spacecraft & Rockets*, Vol. 50, No. 5, 2013, pp. 917–926.

[28] Park, C., Jaffe, R. L., and Partridge, H., "Chemical-Kinetic Parameters of Hyperbolic Earth Entry," *Journal of Thermophysics and Heat Transfer*, Vol. 15, No. 1, 2001, pp. 76–90.

[29] Helber, B., Chazot, O., Magin, T., and Hubin, A., "Space and Time-Resolved Emission Spectroscopy of Carbon Phenolic Ablation in Air and Nitrogen Plasmas," AIAA Paper 2013–2270, 2013.

[30] Johnston, C. O., Gnoffo, P. A., and Mazaheri, A., "Influence of Coupled Radiation and Ablation on the Aerothermodynamic Environment of Planetary Entry Vehicles," VKI Lecture STO-AVT-218, 2013.

[31] Mazaheri, A., Gnoffo, P. A., Johnston, C. O., and Kleb, B., "LAURA Users Manual," NASA TM 2010-216836, 2010.

[32] Gnoffo, P. A., Gupta, R. N., and Shinn, J. L., "Conservation Equations and Physical Models for Hypersonic Air Flows in Thermal and Chemical Nonequilibrium," NASA TP 2867, Feb. 1989.

[33] Gnoffo, P. A., Weilmuenster, K. J., Hamilton, H. H., Olynick, D. A., and Venkatapathy, E., "Computational Aerothermodynamic Design Issues for Hypersonic Vehicles," *Journal of Spacecraft & Rockets*, Vol. 36, No. 1, 1999, pp. 21–43.

[34] Gnoffo, P. A., "An Upwind-Biased, Point-Implicit Relaxation Algorithm for Viscous, Compressible Perfect-Gas Flows," NASA TP 2953, Feb. 1990.

[35] Mcbride, B. J., Zehe, M. J., and Gordon, S., "NASA Glenn Coefficients for Calculating Coefficients for Calculating Thermodynamic Properties of Individual Species," NASA TP 2002–211556, 2002.

[36] Wright, M. J., Bose, D., Palmer, G., and Levin, E., "Recommended Collision Integrals for Transport Property Computations 1: Air Species," *AIAA Journal*, Vol. 43, No. 12, 2005, pp. 2558–2564.

[37] Wright, M. J., Hwang, H., and Schwenke, D. W., "Recommended Collision Integrals for Transport Property Computations Part 2: Mars and Venus Entries," *AIAA Journal*, Vol. 45, No. 1, 2007, pp. 281–288.

[38] Svhehla, R. A., "Estimated Viscosities and Thermal Conductivities of Gases at High Temperatures," NASA TR R 142, 1962.

[39] Johnston, C. O., Gnoffo, P. A., and Mazaheri, A., "A Study of Ablation-Flowfield Coupling Relevant to the Orion Heatshield," *Journal of Thermophysics and Heat Transfer*, Vol. 26, No. 2, 2012, pp. 213–221.

[40] Martin, A. and Boyd, I., "CFD Implementation of a Novel Carbon-Phenolic-in-Air Chemistry Model for Atmospheric Re-Entry," AIAA Paper 2011–0143, 2011.

[41] Park, C., *Nonequilibrium Hypersonic Aerothermodynamics*, Wiley, 1st ed., 1990.

[42] Bourdon, A. and Vervisch, P., "Study of Low-Presure Nitrogen Plasma Boundary Layer over a Metallic Plate," *Physics of Plasmas*, Vol. 4, No. 11, 1997, pp. 4144–4157.

[43] Fujita, K., Yamada, T., and Ishii, N., "Impacts of Ablation Gas Kinetics on Hyperbolic Entry Radiative Heating," AIAA Paper 2006–1185, Jan. 2006.

[44] Bose, D. and Candler, G. V., "Thermal Rate Constants of the O_2+N↔NO + O Reaction based on the $^2A'$ and $^4A'$ Potential Energy Surfaces," *Journal of Chemical Physics*, Vol. 16, No. 107, 1997, pp. 6136–6145.

[45] Park, C., "Review of Chemical-Kinetic Problems for Future NASA Missions, I: Earth Entries," *Journal of Thermophysics and Heat Transfer*, Vol. 7, No. 3, 1993, pp. 385–398.

[46] Teulet, P., Gonzalez, J. J., Mercado-Cabrera, A., Cressault, Y., and Gleizes, A., "One-Dimensional Hydro-Kinetic Modeling of the Decaying Arc in Air-PA66-Copper Mixtures: I. Chemical Kinetics, Thermodynamics, Transport and Radiative Properties," *Journal of Physics D: Applied Physics*, Vol. 42, 2009, pp. 1–15.

[47] Johnston, C. O., Brandis, A. M., and Sutton, K., "Shock Layer Radiation Modeling and Uncertainty for Mars Entry," AIAA Paper 2012–2866, 2012.

[48] Ibragimova, L. B., "Recommended Rate Constants of CO + O_2 – Reversible – CO_2 + O Reactions," *Khim. Fiz.*, Vol. 10, 1991, pp. 307–310.

[49] Park, C., Howe, J. T., Jaffe, R. L., and Candler, G. V., "Review of Chemical-Kinetic Problems for Future NASA Missions, II: Mars Entries," *Journal of Thermophysics and Heat Transfer*, Vol. 8, No. 1, 1994, pp. 9–23.

[50] Gokcen, T., "N_2-CH_4-Ar Chemical Kinetic Model for Simulations of Atmospheric Entry to Titan," AIAA Paper 2004–2469, July 2004.

[51] Gnoffo, P. A., Johnston, C. O., and Thompson, R. A., "Implementation of Radiation, Ablation, and Free-Energy Minimization in Hypersonic Simulations," *Journal of Spacecraft & Rockets*, Vol. 47, No. 2, 2010, pp. 481–491.

[52] Mazaheri, A., Gnoffo, P. A., Johnston, C. O., and Kleb, B., "LAURA Users Manual," NASA TM 2010-216836, 2010.

[53] Johnston, C. O., Hollis, B. R., and Sutton, K., "Spectrum Modeling for Air Shock-Layer Radiation at Lunar-Return Conditions," *Journal of Spacecraft & Rockets*, Vol. 45, Sep.-Oct. 2008, pp. 865–878.

[54] Johnston, C. O., Hollis, B., and Sutton, K., "Non-Boltzmann Modeling for Air Shock Layers at Lunar Return Conditions," *Journal of Spacecraft & Rockets*, Vol. 45, Sep.-Oct. 2008, pp. 879–890.

[55] Johnston, C. O., Gnoffo, P. A., and Sutton, K., "Influence of Ablation on Radiative Heating for Earth Entry," *Journal of Spacecraft & Rockets*, Vol. 46, No. 3, 2009, pp. 481–491.

[56] Chen, Y. K. and Milos, F. S., "Ablation and Thermal Response Program for Spacecraft Heatshield Analysis," *Journal of Spacecraft & Rockets*, Vol. 36, No. 3, 1999, pp. 465–483.

[57] Amar, A., Blackwell, B., and Edwards, J., "Development and Verification of a One-Dimensional Ablation Code Including Pyrolysis Gas Flow," *Journal of Thermophysics and Heat Transfer*, Vol. 23, No. 1, 2009, pp. 59–71.

[58] MacLean, M., Marschall, J., and Driver, D., "Finite-Rate Surface Chemistry Model, II, Coupling to Viscous Navier-Stokes Code," AIAA Paper 2011–3784, 2011.

[59] Keenan, J. A. and Candler, G., "Simulation of Graphite Sublimation and Oxidation under Re-Entry Conditions," AIAA Paper 1994–2083, 1994.

[60] Candler, G., "Nonequilibrium Processes in Hypervelocity Flows: An Analysis of Carbon Ablation Models," AIAA Paper 2012–0724, 2012.

[61] Park, C., "Calculation of Stagnation-Point Heating Rates Associated with Stardust Vehicle," *Journal of Spacecraft & Rockets*, Vol. 44, No. 1, 2007, pp. 24–32.

[62] Stackpoole, M., Sepka, S., Cozmuta, I., and Kontinos, D., "Post-Flight Evaluation of Stardust Sample Return Capsule Forebody Heatshield Material," AIAA Paper 2008–1202, 2008.

[63] Beerman, A., "The Effects of Finite-Rate Reactions at the Gas/Surface Interface in Support of Thermal Protection System Design," Ph.d. dissertation, 2011.

[64] Alkandry, H., Boyd, I., and Martin, A., "Coupled Flowfield Simulations of Charring Ablators with Nonequilibrium Surface Chemistry," AIAA Paper 2013–2634, 2013.

[65] Martin, A. and Boyd, I., "Modeling of Heat Transfer Attenuation by Ablative Gases During Stardust Re-Entry," AIAA Paper 2012–0814, 2012.